Improving Hot-Spot Pressure and Demonstrating Ignition Hydrodynamic Equivalence in Cryogenic Deuterium–Tritium Implosions on OMEGA

Introduction

To ignite the deuterium–tritium (DT) fuel in an inertial confinement fusion[1,2] (ICF) implosion, the ion temperature and areal density of the central, lower-density region (hot spot) of the compressed DT fuel assembly must be sufficient to create self-heating by alpha particles produced as a result of fusing D and T. A typical ICF target consists of a higher-density shell filled with a lower-density fuel vapor. The shell has outer layers of ablator materials and an inner layer of frozen DT fuel. To compress the main fuel and initiate burn, the shell is accelerated inward by a temporally shaped pressure drive created by laser energy that is delivered either directly to the target (direct drive) or indirectly by converting its energy to x rays inside a hohlraum (indirect drive).[1,2]

The peak hot-spot pressure is a critical parameter in ICF implosions. It determines the minimum shell kinetic energy required to create an igniting hot spot. This follows from a simple argument[2] that if the shell's kinetic energy is converted into the internal energy of the hot spot at stagnation, $E_k \rightarrow p_{max} R_{hs}^3$, then $E_k \sim (\rho R_{hs})^3 T^3 / p_{max}^2$, where R_{hs}, $p_{max} \sim \rho T/m_i$, ρ, and T are the hot-spot radius, maximum pressure, mass density, and temperature, respectively, and m_i is the average ion mass. Since the hot spot must satisfy[1–3]

$$(\rho R_{hs}) \times T > 0.3 \, \text{g/cm}^2 \times 5 \, \text{keV} \qquad (1)$$

to ignite, the fuel's kinetic energy must exceed a threshold value $E_k > E_{k,min}$, which depends on the peak pressure

$$E_{k,min} \sim p_{max}^{-2}. \qquad (2)$$

Equation (2) shows that achieving higher pressures in the hot spot relaxes the requirement for the shell's kinetic energy and the laser drive energy. Equation (1) sets the requirement for the hot-spot pressure in an igniting target. Since $p = (1 + Z)\rho T/m_i$ (for DT fuel, $Z = 1$ is the ion charge, $m_i \simeq 2.5 \, m_p$ is the average ion mass, and m_p is the proton mass), Eq. (1) gives

$$p_{hs} > 200 \, \text{Gbar} \left(\frac{50 \, \mu\text{m}}{R_{hs}}\right). \qquad (3)$$

The peak pressure also determines the neutron yield for subigniting ICF implosions. Indeed, the DT fusion reaction rate is $dn_i/dt \sim V_{hs} \times n_i^2 \times \langle \sigma v \rangle$ and the reaction cross section is $\langle \sigma v \rangle \sim T^{4.5}$ (at temperatures $T \sim 2$ to 4 keV, which are typical for sub-ignition ICF implosions). This leads to a total neutron yield of

$$Y \sim V_{hs} \times p_{max}^2 \times T^{2.5} \times \Delta t_{burn}, \qquad (4)$$

where n_i is the ion density, V_{hs} is the hot-spot volume, and Δt_{burn} is the burn duration. Using the adiabatic condition for the hot spot[3,4] $p \sim V_{hs}^{-5/3}$ (see also the discussion later in the text), Eq. (4) becomes

$$Y \sim p_{max}^{7/5} \times T^{2.5} \times \Delta t_{burn}. \qquad (5)$$

Equation (5) shows that higher hot-spot pressures lead to higher target yields.

The maximum pressure depends mainly on the following two effects: first, the conversion efficiency of the shell's kinetic energy into the hot-spot internal energy at shell stagnation; second, the hot-spot size since larger hot-spot volumes lead to smaller peak pressures for a given hot-spot internal energy E_{int}, $p_{max} \sim E_{int}/V_{hs}$. The first effect depends on the fraction of shell mass that stagnates at peak compression. At the beginning of shell deceleration [see Fig. 137.15(a)], the pressure of the central vapor region of an imploding target (which, together with the material ablated from the inside of the shell during acceleration, forms a hot spot at the peak compression) exceeds the shell pressure and an outgoing shock wave is formed at the inner edge of the shell. The vapor (hot-spot) pressure increases while the inner part of the shell converges, performing the pdV work on the vapor region. The inward shell motion is limited
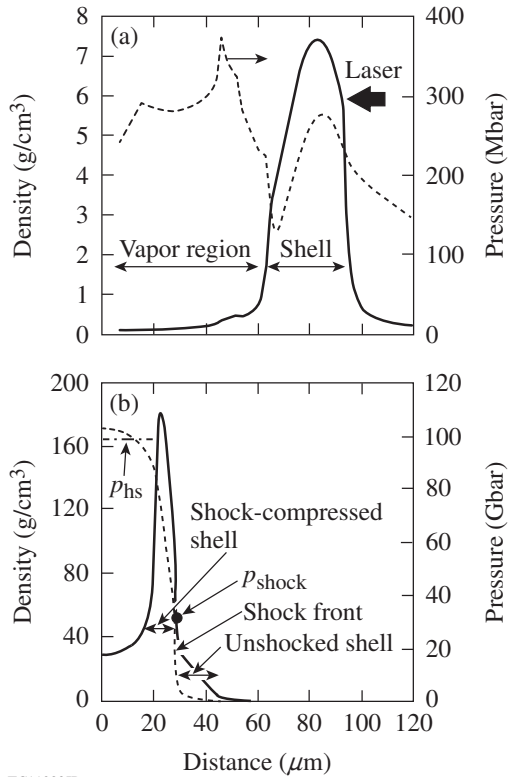
Figure 137.15
The mass-density (solid lines, left axes) and pressure (dashed lines, right axes) profiles at (a) the beginning of shell deceleration and (b) the maximum hot-spot compression for OMEGA cryogenic targets.

by the deceleration force caused by the pressure gradient in the shock-compressed region [see Fig. 137.15(b)]. This pressure gradient is determined first by the pressure behind the shock front (which depends on density ρ and velocity v of the incoming shell ahead of the shock, $p_{shock} \sim \rho v^2$) and second, by the hot-spot pressure, which depends on the hot-spot convergence ratio $p_{hs} \sim V_{hs}^{-5/3}$. If two implosions are considered where the shells have different ρv^2, the pressure behind the shock is lower and the pressure gradient (for a given hot-spot volume) is higher in the shell with a smaller ρv^2. This shell, therefore, experiences a stronger deceleration force, leading to a larger hot-spot volume at stagnation. The amount of shell material overtaken by the outgoing shock is smaller in this case, resulting in a reduced fraction of the shell's kinetic energy being converted into hot-spot internal energy. Since the shell's deceleration depends on the density of the incoming shell, the excessive decompression of the shell by either the Rayleigh–Taylor (RT) instability growth[5,6] or preheat caused by radiation and suprathermal electrons must be prevented.

Predicting the evolution of the hot-spot pressure using hydrodynamic code simulations requires accurate modeling of many physical processes that take place during the target implosion. It is essential, therefore, to validate code predictions of key target-performance characteristics at each stage of the implosion against the experimental data. In addition, experiments can help to identify new physical phenomena (not included in the code simulations) that limit target performance. For such purposes, cryogenic DT capsules are being imploded on the OMEGA Laser System[7] using direct-drive laser illumination. The targets are 7.3- to 12-μm-thick deuterated plastic (CD) shells with outer diameters of 860 μm and 40- to 65-μm-thick cryogenic DT layers. These targets are driven using single and multiple-picket pulses[8] with laser energies of 23 to 27 kJ$_{UV}$ at a peak intensity of 0.4 to 1×10^{15} W/cm^2, reaching implosion velocities (defined as the peak mass-averaged shell velocity) of 2.2 to 4×10^7 cm/s.

This article describes recent progress in understanding cryogenic implosion performance on OMEGA. The following sections (1) describe the cryogenic target designs and the experiments carried out to validate one-dimensional (1-D) implosion parameters; (2) discuss target performance; (3) present hydrodynamic modeling results; and (4) discuss the performance degradation mechanisms, where we also present the strategies for demonstrating the ignition hydrodynamic equivalence on OMEGA, followed by the conclusions.

**Target Designs and Validation
of 1-D Implosion Parameters**
This section describes the cryogenic target designs and discusses the experimental campaigns carried out on OMEGA to validate the key predicted implosion parameters. The simulation results discussed here are obtained using the 1-D hydrocode *LILAC*.[9] These simulations include nonlocal electron thermal transport[10] and the cross-beam energy transfer model.[11–13]

The compression of cryogenic DT fuel is studied for a range of shell adiabat values of $1.5 < \alpha < 6$ [adiabat α is defined as a ratio of the shell pressure to Fermi-degenerate pressure at shell density (see **Target Performance**, p. 23, for more details)], implosion velocities, and the peak laser intensities. Implosion velocity is controlled by varying the CD thickness in a range from 7.2 to 12 μm and an ice thickness from 40 to 65 μm.

Two OMEGA cryogenic target designs are shown in Fig. 137.16. The shell adiabat and the in-flight aspect ratio (IFAR) in implosions are controlled by changing the energies
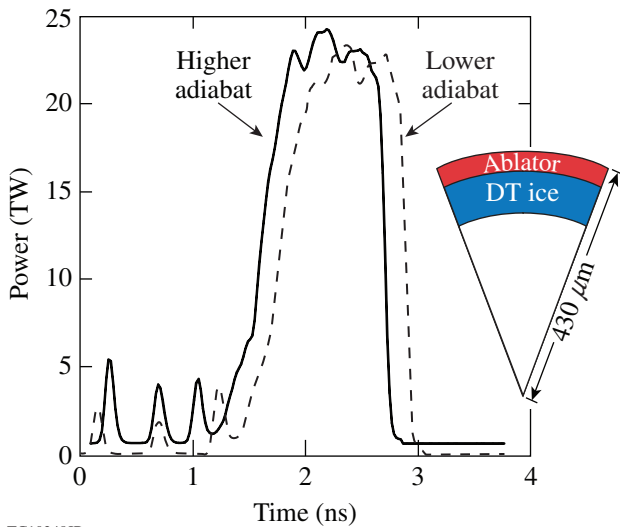
Figure 137.16

Lower- (dashed line) and higher- (solid line) adiabat OMEGA cryogenic designs. Fuel adiabat and in-flight aspect ratio (IFAR) are controlled by changing the energies and separating the lower-intensity pickets. The inset shows target dimensions.

and separating of intensity pickets ahead of the main drive pulse. The lower-adiabat design, shown as a dashed line in Fig. 137.16, has lower-intensity pickets and larger picket-to-picket and picket-to-main-pulse separations.

The plastic overcoat is ablated during the main drive pulse either fully or partially, depending on its thickness. For a given laser energy, there is an optimum CD layer thickness that maximizes the drive (ablation) pressure. This is determined by the interplay of the laser absorption efficiency, radiation losses, electron thermal conduction from the laser-absorption region to the ablation front, and ablation efficiency.

Inverse bremsstrahlung *absorption*[2] is proportional to the average square of the ion charge $\langle Z^2 \rangle$. Consequently, having CD plasma in the laser-deposition region is beneficial for the overall laser absorption because $\langle Z^2 \rangle_{CD} / \langle Z^2 \rangle_{DT} \simeq 18.5$. The higher absorption also leads to a larger coronal temperature and an increased threshold for the two-plasmon–decay (TPD) instability.[14,15] Furthermore, the higher average ion charge $\langle Z \rangle$ and the low fraction of hydrogen atoms in the plasma corona give an additional reduction in TPD growth because of the lower damping rates of ion-acoustic waves.[16] A thicker CD layer also shields the main fuel against radiation preheat from the plasma corona (despite the small opacity of DT, calculations indicate that the amount of radiation from the plasma corona absorbed in the main fuel is sufficient to raise the fuel adiabat by 30% to 50% during target acceleration).

Using ablator materials with higher $\langle Z^2 \rangle$, on the other hand, leads to larger *radiation losses*. Higher-Z materials also reduce the *heat conduction* from the plasma region, where laser energy is absorbed to the ablation front since the thermal conductivity is proportional to $\langle Z \rangle / \langle Z^2 \rangle$. This reduces the mass ablation rate and the ablation pressure.

The *ablation efficiency*, which depends on the ratio of atomic weight A and the averaged ion charge $\langle Z \rangle$, is higher in DT. This dependence follows from the steady-state ablation model,[17] where the incoming absorbed laser power flux (laser intensity) I is balanced by the outgoing energy flux of expanding plasma flow, ρv^3. Here, ρ is the plasma mass density and v is the expansion velocity. Such a model predicts the ablation-pressure and the mass-ablation-rate scalings to be $p_a \sim I^{2/3} (A/Z)^{1/3}$ and $\dot{m} \sim I^{1/3} (A/Z)^{2/3}$, respectively. Since $(A/Z)_{DT} / (A/Z)_{CH} \simeq 1.25$, the ablation pressure and mass ablation rate, as a fraction of absorbed laser energy, are higher in DT by 8% and 16%, respectively.

Considering these competing effects leads to the conclusion that absorbing the laser energy in CD and ablating DT result in a higher ablation pressure. Since the ablation and absorption regions are spatially separated, an optimum CD thickness for which the ablation pressure is maximized requires the ablation front to propagate in DT while the ablated CD plasma is still present in the laser-deposition region. For an OMEGA-scale laser system, the optimum CD thickness is ~7.5 to 8 μm. This is shown in Fig. 137.17, where the ablation pressure is plotted as a function of the CD thickness for targets with a fixed shell mass and a different ratio of CD to DT layer thicknesses. The squares in the figure represent the ablation pressure calculated
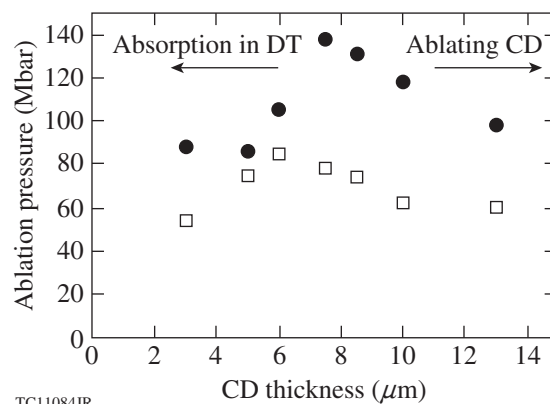
Figure 137.17

Simulated ablation pressure versus the initial CD thickness plotted at the beginning of the shell acceleration (squares) and when the shells have converged by a factor of 2.5 (circles).

at the beginning of the shell acceleration and the circles represent pressures when the shell has converged by a factor of 2.5. The CD thickness that maximizes the ablation pressure changes from ~6 μm earlier in the pulse to 7.5 μm at later times. This change occurs because a CD layer thicker than 6.5 μm is still being ablated at earlier times, resulting in a lower rocket efficiency. By the time the shell has converged by a factor of 2.5, a CD layer thinner than ~10 μm is completely ablated, resulting in an increased rocket efficiency. If the initial CD thickness is less than 7 μm, however, the ablated DT plasma expands into the laser-absorption region, significantly reducing the absorption fraction $\left(\text{as a result of a reduced }\langle Z^2\rangle\right)$.

Since the physics of the ablatively driven implosions is complex, it is important to verify that the key implosion parameters are modeled correctly. The predicted ablation pressure and the mass ablation rate are validated by comparing the simulated shell trajectory, the power and spectrum of the scattered laser light, and timing of the neutron-production history (bang time) with the data. The shell trajectory is verified by comparing the measured spatial profile of the x-ray emission from plasma corona[18] with the predictions. Figure 137.18(a) shows a schematic of the x-ray emission map together with a lineout of the self-emission image as measured by an x-ray framing camera. Figure 137.18(b) plots the simulated electron density (solid line), electron temperature (dashed line), and the line-integrated self-emission projected on the detector plane (dotted line) for a typical cryogenic implosion on OMEGA. This figure shows that the ablation front is in very close proximity to the peak in the x-ray emission. Therefore, comparing the measured and simulated positions of the peak or the inner edge of the emission profile provides a good measure of the accuracy in predicting the ablation-front trajectory. Taking the time derivative of the ablation-front trajectory gives the ablation-front velocity.[19] It peaks at a value smaller than the implosion velocity v_{imp} since the convergence effects move the location of the peak pressure from the ablation front to the inner part of the shell, creating a force that decelerates only the ablation-front region while the average shell velocity continues to increase (see **Implosion Modeling**, p. 27, for more details). Figure 137.19 shows, as an example, (a) one of the 16 gated self-emission images taken during a cryogenic implosion, together with (b) inferred ablation-front trajectory, and (c) its velocity. There is excellent agreement between the simulation results and the measurements.

Laser absorption and the ablated plasma evolutions are inferred by measuring the power and spectrum of the scattered
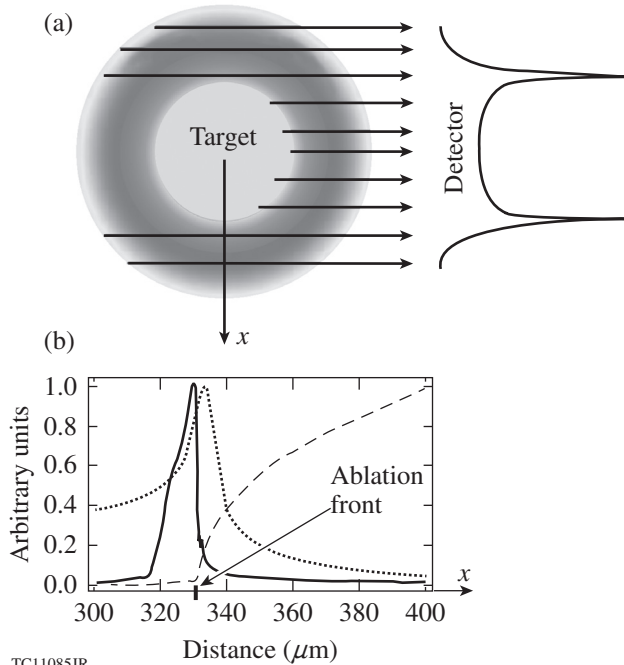

Figure 137.18
(a) Schematic of the coronal x-ray emission and a lineout of the self-emission image as measured by an x-ray framing camera. (b) Simulated electron density (solid line), electron temperature (dashed line), and the path-integrated plasma self-emission (dotted line) projected on the detector plane.
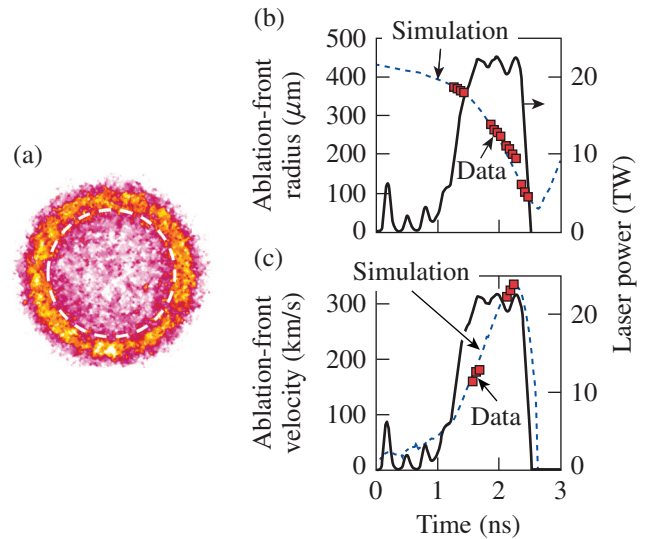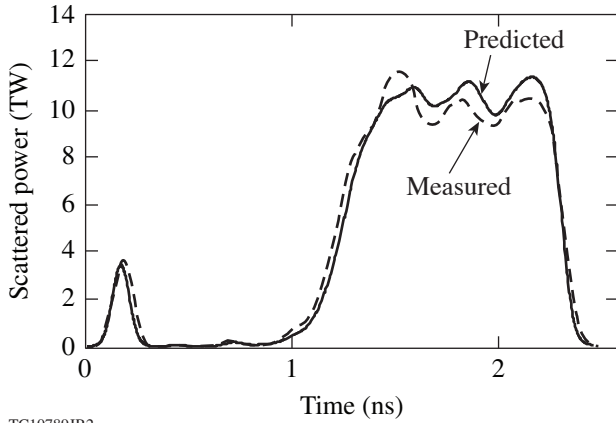

Figure 137.19
(a) Self-emission image as measured by the x-ray framing camera. The white dashed circle marks the position of the inner edge in the emission profile. (b) The predicted ablation-front position (dashed line) and the measured location of the inner edge of self-emission (red squares) for the OMEGA cryogenic implosion (shot 70030). (c) The predicted ablation-front velocity (dashed line) and the velocity of the measured inner edge of self-emission profile (red squares). The laser pulse is shown as a solid line.

light.[20] Figure 137.20 shows the measured scattered power (dashed line), which agrees very well with predictions (solid line). The measured and predicted laser-absorption fractions are 55±4% and 55%, respectively.


TC10789JR2

Figure 137.20
The measured (dashed line) and predicted (solid line) scattered-light power for the OMEGA cryogenic implosion (shot 69514).

The measured time-resolved scattered-light spectrum is compared with the simulations in Fig. 137.21. The temporal shifts in the scattered laser light are caused by changing the optical path length in the plasma traversed by the laser rays. *LILAC* modeling of the scattered-light spectrum includes calculating frequency shifts[21] and convolving the results with the incident laser spectrum resulting from smoothing by spectral dispersion (SSD).[22] Except for a discrepancy at the beginning of the main drive, both spectra agree very well.

The temporal behavior of the spectrum can be understood by using a simplified description based on a frequency shift of the light reflected from a moving surface (which corresponds to the critical surface where the electron density is equal to $n_{cr} \simeq 9 \times 10^{21}$ cm^{-3}). The velocity of the critical surface is plotted in Fig. 137.22(a). At the early times, $t < 0.3$ ns, this velocity is positive, making the reflecting surface move toward the observer and causing a blue shift in the spectrum. Later, as the laser intensity begins to rise during the main pulse, the velocity rapidly changes to a negative value, causing a red shift in the spectrum at $t \simeq 1.3$ ns. An additional sharp velocity shift occurs at $t \simeq 1.9$ ns. This is caused by the onset of the laser
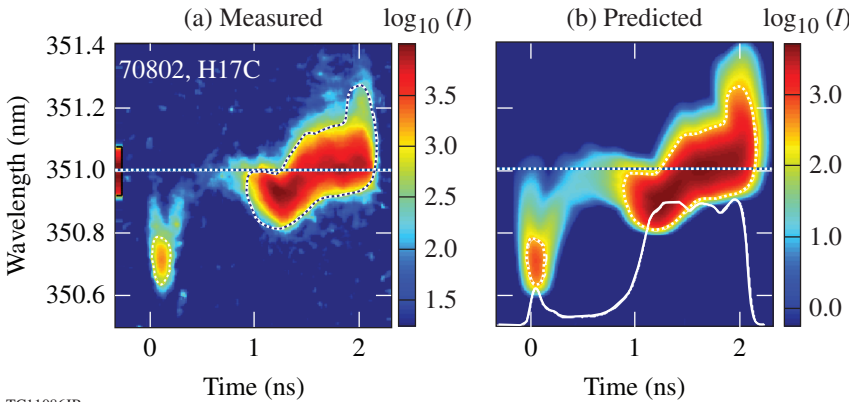
TC11086JR

Figure 137.21
The (a) measured and (b) predicted scattered-light spectra for a OMEGA cryogenic implosion (shot 70802). The white dashed lines mark the 50% simulated intensity contour. They are also shown on the measured spectrum to help compare with the data. The pulse shape is shown with the solid white line on the simulated image.
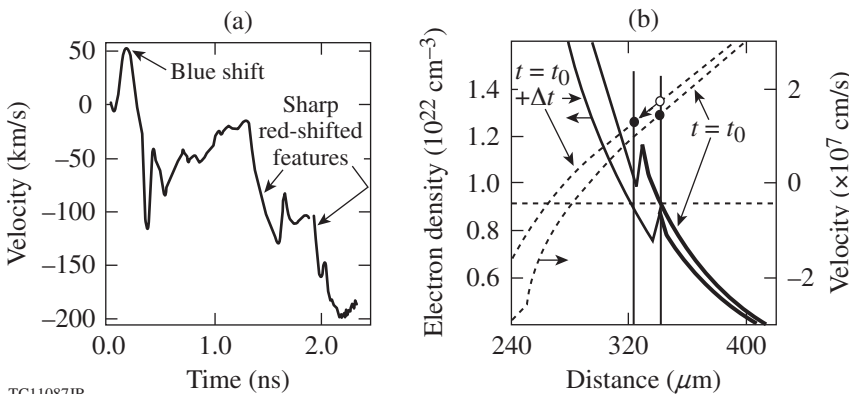
TC11087JR

Figure 137.22
(a) Simulated velocity of the critical surface. The positive velocity early in the pulse ($t \simeq 0.1$ to 0.3 ns) results in a blue-shifted part of the scattered-light spectrum (see Fig. 137.21). The sharp velocity variations at $t \simeq 1.3$ and $t \simeq 1.9$ ns lead to the sharp red-shifted features in the spectrum. The pulse shape is shown in Fig. 137.21(b) with the white line. (b) The electron density (solid lines) and flow velocity (dashed lines) in a cryogenic implosion as predicted by *LILAC*. The two vertical lines indicate the positions of the critical electron density at two different times during the implosion.

deposition in the ablated DT plasma and a mismatch in the electron density across the CD/DT interface, which is a consequence of the continuity in pressure (resulting from momentum conservation) and the electron and ion temperatures (because of thermal conduction):

$$n_{e,DT} = n_{e,CD} \frac{1 + T_i/(Z_{CD} T_e)}{1 + T_i/(Z_{DT} T_e)} < n_{e,CD}, \qquad (6)$$

where $n_{e,CD(DT)}$ and $Z_{CD(DT)}$ are the electron density and the ion charge of the plasma on the CD(DT) side of the CD–DT interface, and T_i and T_e are the ion and electron temperatures, respectively. This is illustrated in Fig. 137.22(b), where the electron density profiles (solid lines) predicted by *LILAC* are plotted at two different times for a typical cryogenic implosion. After the electron density in the expanding CD plasma drops below the critical density at the CD/DT interface, the critical surface position jumps farther inward. This is shown in Fig. 137.22(b) as the critical density (dotted horizontal line) at $t = t_0$ is inside the CD plasma at $R \simeq 340$ μm. At $t = t_0 + \Delta t$, the critical density moves into DT at $R \simeq 324$ μm. The separation between the two density profiles in the CD region is only ~5 μm. Therefore, an additional ~10-μm shift in the critical-surface position is caused by a transition from the CD to DT plasma. As the CD/DT interface travels through the plasma corona region toward the lower electron densities (because of the ablated-plasma expansion), T_i becomes much smaller than T_e (the electron–ion energy exchange rate is reduced at lower plasma densities), leading to continuity in the electron density. When the interface is at the critical density, however, $T_i \simeq T_e/2$ and $n_{e,DT} < n_{e,CD}$.

The jump in the position of n_{cr} leads to a reduction in the expansion flow velocity [shown with the dashed lines in Fig. 137.22(b)] at the critical density. Such a reduction is caused by the continuity in the mass flux, ρv (where $\rho = A m_p n_e/Z$, A is atomic mass, and m_p is proton mass). Without the material change, the velocity at the critical density would change from a value marked by the solid circle at $t = t_0$ to the open circle at $t = t_0 + \Delta t$. With the transition from CD to DT, the flow velocity is reduced to a value marked by the solid circle at $R = 324$ μm:

$$v_{DT}(n_e) = v_{CD}(n_e) \frac{(A/Z)_{CH}}{(A/Z)_{DT}} \simeq 0.8 \, v_{CD}(n_e). \qquad (7)$$

The reduction in the expansion velocity at the critical surface causes the critical surface to move inward faster, lead-

ing to a sharp variation in the critical-surface velocity [see Fig. 137.22(a)] and the red-shifted feature in the scattered-light spectrum at $t \simeq 1.9$ ns. Figure 137.21 shows that the observed red-shifted part in the spectrum at the end of the pulse is delayed and has a somewhat slower rise than that predicted by *LILAC*. This suggests a more-gradual transition from CD to DT at the interface, likely a result of mixing of CD and DT in the expanding plasma corona.

In summary, the 1-D dynamics of cryogenic imploding shells is modeled correctly using *LILAC*. This is achieved by including the nonlocal electron thermal transport[10] and the cross-beam energy transfer[12] models. This result is very important since the measured performance degradation relative to the 1-D predictions can be attributed to the multidimensional effects, mainly the growth of hydrodynamic instabilities.

Target Performance

Target performance is quantified by several key observables, including the neutron-averaged areal density, neutron yield, neutron-production history, neutron-average ion temperature, and hot-spot pressure.
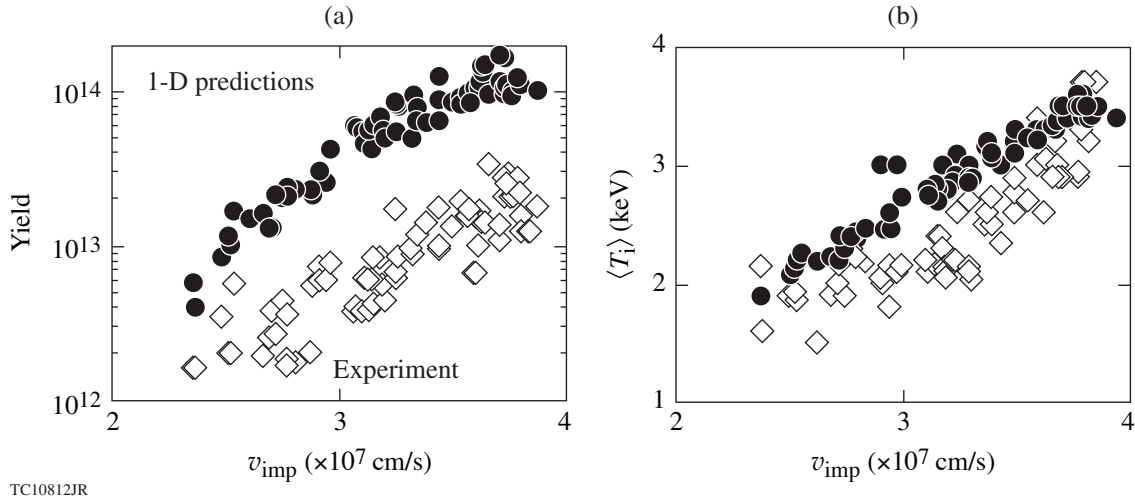
1. Neutron Yield and Ion Temperature

Figure 137.23 shows the calculated and measured neutron yields and the neutron-averaged ion temperatures as functions of the calculated implosion velocity. The implosion velocity in the simulations is defined as the peak in mass-averaged shell velocity:

$$v_{imp} = \max_{time}\left(\left| v_{shell} \right|\right), \quad v_{shell} = \frac{\int_{r_1}^{r_2} \rho(r,t) v(r,t) r^2 \, dr}{\int_{r_1}^{r_2} \rho(r,t) r^2 \, dr}, \qquad (8)$$

where r_1 and r_2 are the positions where the shell density equals ρ_{max}/e at the inner and outer sides from shell peak density, and ρ and v are mass density and flow velocity, respectively.

The neutron-averaged ion temperature is calculated using the width of the neutron spectrum f_n, which includes both the thermal and bulk velocity broadenings:[23–25]

$$\langle f_n(E) \rangle_V = \frac{\int dV n_1 n_2 \langle \sigma v \rangle_{12} e^{-[\alpha(E) - M_a \cos\theta]^2}}{\int dV n_1 n_2 \langle \sigma v \rangle_{12}}, \qquad (9)$$

TC10812JR

Figure 137.23
(a) The measured (diamonds) and 1-D predicted (circles) neutron yields; (b) the neutron-averaged ion temperatures for OMEGA cryogenic implosions. The typical error bar for the measured ion temperature is ±4%.

where θ is the angle between flow velocity and the neutron detector, $\langle\sigma v\rangle_{12}$ is the reaction cross section between species 1 and 2, n_1 and n_2 are the ion densities of species 1 and 2, respectively, $\alpha(E) = (E - E_0)/\Delta E$, $M_a = v/c_s$ is the flow Mach number, v is the flow velocity, $c_s = \sqrt{T_i/m_i}$ is the ion sound speed, $m_i = (m_n + m_\alpha)/2$ is the average ion mass of reaction products, $E_0 = m_\alpha/(m_n + m_\alpha)Q$, Q is the nuclear energy released in a fusion reaction ($Q = 17.6$ MeV for D + T reaction), m_n and m_α are the masses of the reaction products (neutron and alpha particle for DT), and

$$\Delta E = 2\sqrt{\frac{m_n T_i E_0}{m_n + m_\alpha}}.$$

Taking the integral over the angles [assuming the spherical symmetry in Eq. (9)] yields

$$\langle f_n(E)\rangle_V = \sqrt{\pi}$$

$$\times \frac{\int_0^R dr\, r^2 n_1 n_2 \langle\sigma v\rangle_{12}\left\{\mathrm{erf}\left[\alpha(E) + M_a\right] - \mathrm{erf}\left[\alpha(E) - M_a\right]\right\}}{4 M_a \int_0^R dr\, r^2 n_1 n_2 \langle\sigma v\rangle_{12}},$$

$$(10)$$

where $\mathrm{erf}(x)$ is the error function and R is the site of the neutron-production region. Integrating Eq. (10) over the neutron-production time and fitting the result with a Gaussian with a full width at half maximum (FWHM) = ΔE_{fit},

$$\int dt\, \langle f_n(E)\rangle_V \xrightarrow{\mathrm{fit}} \exp\left[-4\ln 2\left(\frac{E - E_0}{\Delta E_{\mathrm{fit}}}\right)^2\right],$$

defines an effective temperature

$$\langle T_i\rangle_{n,\mathrm{fit}} = \frac{\Delta E_{\mathrm{fit}}^2}{E_0}\frac{1 + m_\alpha/m_n}{16\ln 2}, \qquad (11)$$

which for DT reactions leads to[25] $\langle T_i\rangle_{n,\mathrm{fit}} = (\Delta E_{\mathrm{fit}}/177)^2$. Both ΔE and T_i in the latter equation are in keV. The ion temperature is inferred in an experiment by measuring the temporal width of the neutron time of flight, Δ_{TOF}. Using the relation between the neutron energy spread ΔE and Δ_{TOF},

$$\frac{\Delta E}{E_0} = 2\frac{\Delta_{\mathrm{TOF}}}{\mathrm{TOF}} \quad \left(\text{where } \mathrm{TOF} = \sqrt{\frac{m_n}{2E_0}}L\right) \qquad (12)$$

in Eq. (11) gives

$$\langle T_i\rangle_{n,\mathrm{exp}} = E_0^2\frac{1 + m_\alpha/m_n}{m_n 2\ln 2}\left(\frac{\Delta_{\mathrm{TOF}}}{L}\right)^2. \qquad (13)$$

For DT, Eq. (13) reduces to

$$\langle T_i\rangle_{n,\mathrm{exp}} = 68\frac{\Delta_{\mathrm{TOF}}^2}{L^2}, \qquad (14)$$

where L is the distance from detector to target in meters and Δ_{TOF} is in nanoseconds.[25]

The predicted neutron yield in Fig. 137.23(a) scales as

$$Y_{1\text{-D}} \sim v_{imp}^6 \alpha^{-0.8}, \qquad (15)$$

while the best fit to the experimental yield gives

$$Y_{exp} \sim v_{imp}^5 \alpha, \qquad (16)$$

where α is defined as the mass-averaged adiabat

$$\alpha = \frac{1}{m_{shk} - m_b} \int_{m_b}^{m_{shk}} \frac{p(m)}{\mu \rho(m)^{5/3}} dm, \qquad (17)$$

calculated using *LILAC*, $dm = 4\pi\rho r^2 dr$ is a differential of the mass coordinate, m_b is the position in the mass coordinate where $\rho(m_b) = \rho_{max}/e$ at the inner shell surface, ρ_{max} is the peak density, m_{shk} is the shell mass (shocked mass) overtaken by the return shock at the time of the peak neutron production (bang time),

$$\mu = \frac{(3\pi^2)^{2/3}}{5} \frac{\hbar^2 Z^{5/3}}{m_e m_i^{5/3}}, \qquad (18)$$

m_i and m_e are the average ion and electron masses, respectively, Z is the average ion charge, and $\hbar$ is the Planck constant. In general, α increases with time during the shell acceleration, mainly because of radiation heating from the plasma corona. In this article, adiabat α is calculated near the beginning of shell acceleration, when $R_a = 2/3\ R_{vapor}$, where R_a is the ablation-front radius and R_{vapor} is the radius (initial radius) of the vapor region of an undriven shell.

The lower-adiabat implosions are predicted to result in higher fuel compression and higher ion temperatures. This leads to higher yields if the multidimensional effects are not taken into account. The target performance in an experiment is strongly degraded, however, as the adiabat is reduced[26] (because of a weaker ablative stabilization and, consequently, the larger growth of the RT instability), leading to a linear dependence of the measured yields on α. Figure 137.24 plots the neutron yields normalized to *LILAC* predictions. As the fuel adiabat gets smaller, the yields drop with respect to the 1-D predictions. This indicates that the shell stability plays a crucial role in determining target performance.
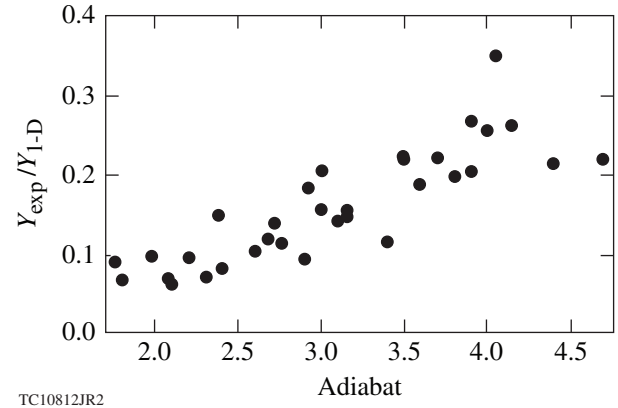

TC10812JR2

Figure 137.24
Experimental yields normalized to *LILAC* predictions. Only data for shells with CD thicknesses of 7.5 to 8.3 μm are shown.

2. Areal Density

In addition to the target yields, the performance degradation is quantified by plotting the neutron-averaged areal-density reductions (with respect to the 1-D predictions) as a function of adiabat and the target IFAR. Here,

$$IFAR = \frac{R_{a,2/3}}{\Delta_{2/3}} \qquad (19)$$

is defined near the beginning of shell acceleration, when the ablation front is at $R_{a,2/3} = 2/3\ R_{vapor}$. The shell thickness Δ is defined as the distance between the inner and outer positions where the shell density equals the initial density of the ablator ($\rho = 1.08$ g/cm^2 for CD). Figure 137.25(a) shows the map of the absolute values of the areal density averaged over two independent measurements using the magnetic recoil spectrometer (MRS)[27] and a highly collimated neutron time-of-flight (nTOF) detector.[28] The black points represent the individual OMEGA shots. The map was created by interpolating the ρR values between the experimental points.

As the fuel adiabat gets smaller and the shell IFAR larger, the measured ρR drops with respect to the 1-D predictions. Figure 137.25(b) shows that a stability boundary, defined by

$$IFAR_{boundary} \simeq 20(\alpha/3)^{1.1}, \qquad (20)$$

separates the region where more than 85% of the 1-D–predicted areal density is observed (on the right side from the boundary) and the region where shell compressibility is compromised by the nonuniformity growth and the measured areal density is reduced.
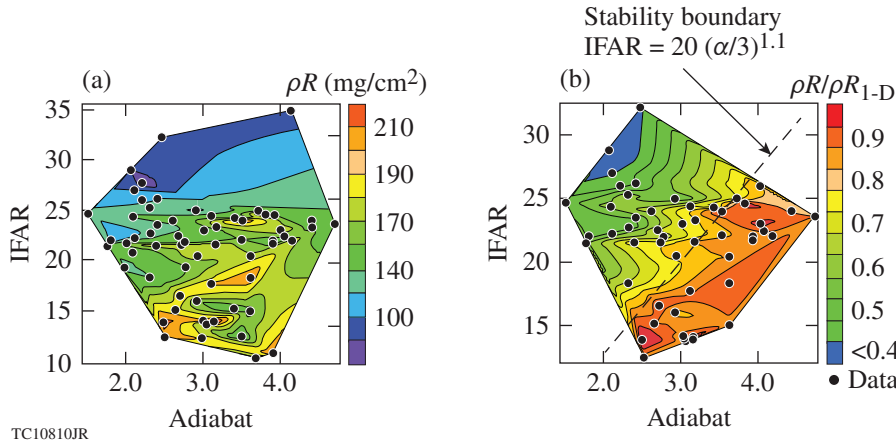
TC10810JR

Figure 137.25
(a) Contour map of the measured areal density as a function of calculated adiabat and IFAR. The contours represent a linear fit to the experimental data (black points). (b) Contour map of the measured areal density normalized to *LILAC* predictions. The dashed line (a stability boundary) separates the region where more than 85% of the 1-D–predicted areal density is observed and the region where the shell areal density is significantly reduced because of the hydrodynamic instability growth.

3. Hot-Spot Pressure

The hot-spot pressure evolution in the experiments is estimated using the ratio of the predicted and measured neutron-production histories. With the help of Eq. (5), the neutron-production rate can be written as

$$\dot{N} = \frac{dN}{dt} \sim p_{hs}^{7/5} T_{i}^{2.5}. \tag{21}$$

Then, taking the ratio of the experimental and predicted $\dot{N}$ and using the result to obtain the hot-spot pressure inferred in the experiment p_{hs}^{exp} gives

$$p_{hs}^{exp} \simeq p_{hs}^{theory} \left(\frac{T_{exp}}{T_{theory}} \right)^{-1.8} \left(\frac{\dot{N}_{exp}}{\dot{N}_{theory}} \right)^{-0.7}. \tag{22}$$

The neutron-production measurement is time resolved,[29] while the neutron-averaged ion temperature is a time-integrated quantity. In evaluating Eq. (22), therefore, the time-integrated neutron-averaged temperatures are used in both the measured T_{exp} and predicted T_{theory} ion temperatures. Figure 137.26 shows the temporal evolutions of the measured and 1-D–predicted neutron-production rates; the predictions include the instrumental as well as the thermal and bulk-velocity broadening, as shown in Eq. (10). The calculated and inferred hot-spot pressures are plotted in Fig. 137.27 for two OMEGA shots with similar 1-D implosion parameters ($\alpha \sim 4$). The figure indicates that 35% to 40% of the hot-spot pressures predicted by *LILAC* is achieved in OMEGA cryogenic implosions at these moderate adiabat values. These pressure values are consistent with the results of the hot-spot model described in Ref. 30.
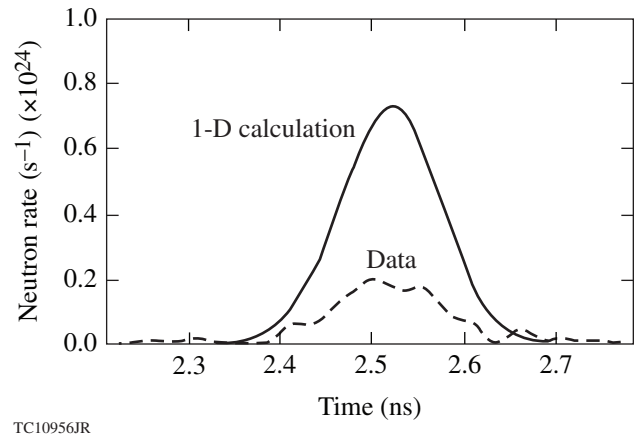

TC10956JR

Figure 137.26
The measured (dashed line) and predicted (solid line) neutron-production histories for an $\alpha = 4$ cryogenic implosion (shot 69514).

The hot-spot pressure evolution for a lower-adiabat implosion ($\alpha \sim 2$) is shown in Fig. 137.28. Although the predicted peak pressure increases to 150 Gbar, the pressure inferred in the experiment is reduced compared to that in the inferred higher-adiabat implosions.

A two-dimensional (2-D) map of the neutron-averaged hot-spot pressures and the ratios of the inferred and predicted pressures is shown in Fig. 137.29. The hot-spot pressure peaks at $\alpha \sim 4$ and an IFAR ~ 22. The pressure is lower in implosions with a smaller IFAR because of the reduced predicted values [lower implosion velocities or higher adiabats lead to lower hot-spot pressures (see **Discussion**, p. 35)]. A reduced pressure for the higher-IFAR implosions is due to a loss in the target stability. This will be discussed in more detail in the next section.

Implosion Modeling

This section describes the analysis of the cryogenic target performance based on 2-D simulations in the next subsection and using simplified analytic models, see p. 28).

1. Integrated Two-Dimensional Simulations

To improve the target performance and demonstrate the ignition hydrodynamic equivalence of cryogenic implosions on OMEGA, it is important to understand the trends in the experi-
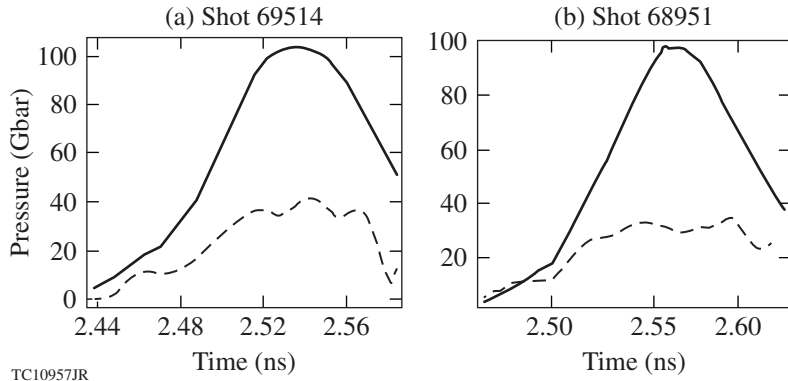

TC10957JR

Figure 137.27
The calculated (solid lines) hot-spot pressure and the pressure inferred (dashed lines) using the measured neutron-production history and ion temperature for two $\alpha \simeq 4$ implosions. The predicted and inferred peaks in the central pressure p_{max} are 100 Gbar and 41 Gbar (shot 69514) and 100 Gbar and 33 Gbar (shot 68951), respectively. The predicted and inferred neutron-averaged hot-spot pressures $\langle p \rangle_n$ are 72 Gbar and 29 Gbar (shot 69514) and 66 Gbar and 24 Gbar (shot 68951), respectively.

TC10958JR

Figure 137.28
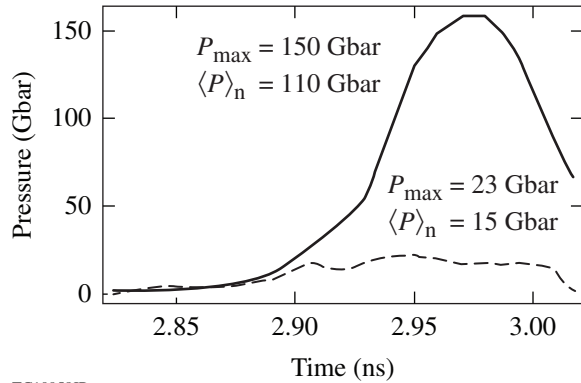The predicted (solid line) and inferred (dashed line) hot-spot pressure for an $\alpha \simeq 2.1$ implosion (shot 69236).
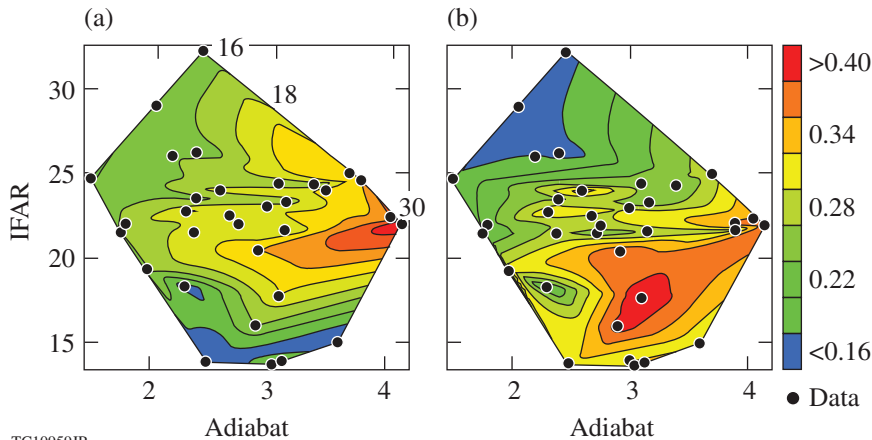

TC10959JR

Figure 137.29
(a) Contour map of the inferred neutron-averaged hot-spot pressure. The constant-pressure contours with $\langle p \rangle_n$ = 16, 18, and 30 Gbar are labeled on the map. (b) Contour map of the inferred pressure normalized to *LILAC* predictions.

mental data shown in Figs. 137.24 and 137.29. As a first step, the 2-D hydrocode *DRACO*[31] was used to calculate the effects of the target-surface roughness, the short-wavelength, single-beam nonuniformity (laser imprint), and the long-wavelength illumination nonuniformities caused by the beam power imbalance, the beam-overlap pattern, the beam mistiming, and target offset. Figure 137.30 shows the simulation results[32] of the mid-adiabat ($\alpha \sim 4$) implosion (OMEGA shot 69514). Table 137.III summarizes the predicted and measured performance parameters. Table 137.III and Fig. 137.30 indicate that the neutron yield, areal density, and burnwidth are in very good agreement with the observables. The size of the x-ray image calculated using the *DRACO* simulation post-processed with the radiative transfer code *Spect3D*[33] is also in good agreement with measurements made using the gated x-ray imager (GMXI).[34]

Simulations of lower-adiabat ($\alpha \sim 2$) implosions, however, fail to reproduce the experimental data. The measured areal densities are significantly lower than the simulated values (by
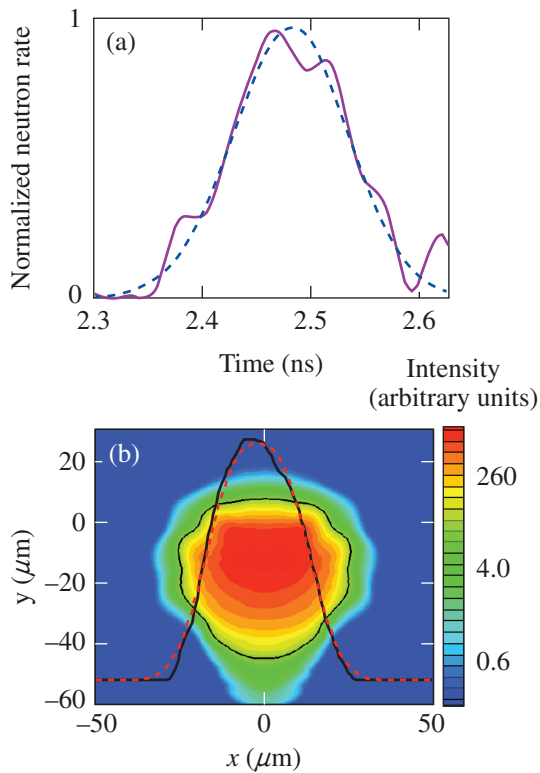
E22296JR

Figure 137.30

(a) Measured (solid line) and simulated using the 2-D hydrocode *DRACO* (dashed line) neutron-production history for a mid-adiabat ($\alpha \sim 4$ shot 69514) implosion. (b) A lineout of the measured time-integrated x-ray emission (red dashed line) and the results of a *DRACO* simulation post-processed using *Spect3D* [shown as a contour map of intensity and a lineout of this map (black line)].

a factor of 1.5 to 2), the experimental burn width is larger by almost a factor of 2, and the size of the x-ray emission region is significantly larger as well. The results of simulations are compared with the data in Table 137.IV.

Table 137.III: Summary of the measured and *DRACO*-calculated target performance parameters for an $\alpha = 4$ cryogenic implosion (shot 69514).

Observables	Simulation	Experiment
Yield ($\times 10^{13}$)	3.9	3.0±0.1
T_i (keV)	3.7	3.6±0.3
ρR (mg/cm^2)	180	175±15
p_{hs} (Gbar)	32	30±5

Table 137.IV: Summary of the measured and *DRACO*-calculated target performance parameters for an $\alpha = 2$ cryogenic implosion (shot 69236).

Observables	Simulation	Experiment
Yield ($\times 10^{13}$)	1.7	1.1±0.1
T_i (keV)	2.9	3.0±0.2
ρR (mg/cm^2)	190	110±13
Burnwidth (ps)	80	115±10
p_{hs} (Gbar)	41	18±5

This limited ability of the hydrodynamic simulations to explain the observables in the low-adiabat implosions on OMEGA is common to that in indirect-drive cryogenic implosions[35] at the National Ignition Facility (NIF).[36] To understand the factors limiting the target performance, it is not sufficient to rely solely on the simulations because of uncertainties in the physical models used in these codes. In addition, not all the sources of the target and illumination nonuniformities can be identified and characterized with the precision required to resolve the performance-relevant spatial scales. Simplified theoretical models can help in developing a physical understanding of the implosion dynamics and failure mechanisms. Such models will be described in the next section.

2. Simplified Models of the Implosion Dynamics

The peak hot-spot pressure can be estimated using the argument that stopping the incoming shell with density ρ_{shell} and velocity v_{imp} by a strong shock requires a shock pressure of

$$p_{max} \simeq 4/3 \rho_{shell} v_{imp}^2 . \tag{23}$$

Using the in-flight shell quantities (an ablation pressure of 100 Mbar, fuel adiabat $\alpha \sim 1$, and shell velocity $v_{imp} = 4 \times 10^7$ cm/s), Eq. (23) gives only

$$p_{max} \simeq 4/3 \left(p_a/2.2\alpha\right)^{3/5} v_{imp}^2$$

$$= 4/3 \left(100\,\text{Mbar}/2.2\right)^{3/5} \left(4 \times 10^7\right)^2 = 21\,\text{Gbar},$$

an order of magnitude lower than the peak pressure predicted in a hydrodynamic code simulation at these conditions. The source of the pressure deficiency in using this simple argument is the spherical convergence effects that are important during the final stages of the hot-spot formation ($\rho_{shell} \gg \rho_{in\,flight}$). The shell convergence increases the density of the incoming shell during the deceleration. Because peak stagnation pressures exceeding 100 Gbar are required in an igniting hot spot, it is crucial to understand the dynamics of shell deceleration and the hot-spot pressure amplification near stagnation.

The hot-spot pressure's dependence on the shell convergence provides a starting point in describing the deceleration dynamics. Since the thermal conduction losses from the hotter central region to the colder shell material are balanced by the internal energy flux of the ablated material back into the hot spot, pressure inside the hot spot is not affected by the ablation and can be calculated using the adiabatic approximation[3] $p_{hs} \sim V_{hs}^{-5/3}$, where V_{hs} is the hot-spot volume. If $V_{hs,0}$ and $p_{hs,0}$ are the volume and pressure of the vapor region at the beginning of shell deceleration, the time evolution of the hot-shot pressure can be described by

$$p_{hs} = p_{hs,0} \left(\frac{V_{hs,0}}{V_{hs}}\right)^{5/3}. \tag{24}$$

As the hot spot approaches stagnation and the electron temperature starts to rise (the electron–ion energy exchange rate increases with the hot-spot density), the hot-spot mass increases because of the mass ablation from the inner part of the shell. Consequently, the temporal behavior of the ventral pressure cannot be described by the central density alone, $p_{hs} \not\propto \rho_{hs}^{5/3}$, even though Eq. (24) is satisfied. The central pressure peaks as the hot-spot volume reaches its minimum value V_{min},

$$p_{max} = p_{hs,0} \left(\frac{V_{hs,0}}{V_{min}}\right)^{5/3}. \tag{25}$$

Calculating the peak central pressure, therefore, reduces to determining the vapor pressure $p_{hs,0}$ at the beginning of the shell's deceleration and the hot-spot volume reduction fraction during deceleration $V_{hs,0}/V_{min}$ [this is related to the hot-spot convergence ratio (CR), $p_{max} \sim CR^5$, in a 1-D implosion].

The shell position and the vapor volume $V_{hs,0}$ at the start of deceleration are the key parameters since the farther the shell moves inward before it begins to decelerate, the higher the shell density ρ_{shell} (because of the convergence effects) and, according to Eq. (23), the higher the maximum pressure ($\rho_{shell} v_{imp}^2$ is larger because of the higher ρ_{shell}). The shell deceleration begins when the vapor pressure, amplified by the shell convergence, exceeds the shell pressure (which is higher for the higher ablation pressures). Therefore, the onset of shell deceleration depends on the vapor and shell pressure evolutions during the shell acceleration. The vapor pressure history will be discussed first.

a. Vapor-pressure evolution. Three main effects contribute to the increase in vapor pressure during the implosion: (1) the compression of the initial vapor mass introduced into the central part of the target during the cryogenic-layer formation; (2) the density rarefaction (material release) at the inner part of the shell during the acceleration; and (3) the excessive nonuniformity growth that leads to the shell breakup, injecting the cold shell and plasma-corona materials into the vapor region. The first contribution can be calculated using the pressure–density relation

$$p_{v,1} = \mu \alpha_v \rho_v^{5/3}, \tag{26}$$

where α_v is the adiabat of the vapor region, $p_{v,1}$ and ρ_v are the vapor pressure and density, respectively, and μ is defined in Eq. (18). The vapor volume V_v gets smaller during the shell's convergence, so the average vapor density increases as

$$p_v = \rho_{v,0} V_{v,0}/V_v, \tag{27}$$

where $\rho_{v,0}$ and $V_{v,0}$ are the density and volume of the vapor region in an undriven target. Neglecting the kinetic effects of ions, the vapor adiabat is determined mainly by shock heating:

$$\alpha_v = \frac{p_{v,shk}}{\mu \rho_{v,shk}^{5/3}}, \tag{28}$$

where $p_{v,shk}$ and $\rho_{v,shk}$ are the pressure and density behind the leading shock that travels in the vapor and μ is defined in Eq. (18). Since the leading shock is strong, $\rho_{v,shk} \simeq 4\rho_{v,0}$;

it can be shown that the relation between the ablation and shock pressures takes the form

$$p_{\mathrm{v,shk}} \simeq p_{\mathrm{a},0} \frac{\rho_{\mathrm{v},0}}{\rho_0} \left\{ 1 + 2\sqrt{5}\left[1 - \left(\frac{\rho_{\mathrm{v},0}}{\rho_0} \right)^{1/5} \right] \right\}, \qquad (29)$$

where $p_{\mathrm{a},0}$ is the ablation pressure at the beginning of shell acceleration and ρ_0 is the initial (undriven) main fuel density ($\rho_0 \simeq 0.25$ g/cm^3 for DT ice). Using Eqs. (26)–(29) gives the vapor adiabat

$$\alpha_{\mathrm{v}} = \frac{p_{\mathrm{a},0}}{4^{5/3} \mu \rho_{\mathrm{v},0}^{2/3} \rho_0} \left\{ 1 + 2\sqrt{5}\left[1 - \left(\frac{\rho_{\mathrm{v},0}}{\rho_0} \right)^{1/5} \right] \right\}, \qquad (30)$$

and the contribution to the vapor pressure related to the convergence of the initial vapor mass becomes

$$p_{\mathrm{v},1} \simeq \frac{p_{\mathrm{a},0}}{4^{5/3}} \frac{\rho_{\mathrm{v},0}}{\rho_0} \left\{ 1 + 2\sqrt{5}\left[1 - \left(\frac{\rho_{\mathrm{v},0}}{\rho_0} \right)^{1/5} \right] \right\} \left(\frac{V_{\mathrm{v},0}}{V_{\mathrm{v}}} \right)^{5/3}. \qquad (31)$$

The convergence effects of the leading shock wave break the validity of Eq. (29) near the target center, so Guderley's solution[37] must be used. The volume of the vapor region where this occurs, however, is small compared to the total vapor volume. A correction to the vapor pressure caused by an increase in the shock strength near the origin, therefore, is small.

Strictly speaking, the shock convergence effects near the target center cannot be described using Guderley's solution either because of ion heating that becomes strong enough to raise the ion temperatures to a few keV at the shock front. The ions in the high-energy tail of the distribution function travel ahead of the shock in this case,[38] preheating the vapor region and raising its adiabat. The higher adiabat leads to an increase in the vapor pressure (for a given vapor mass), causing shell deceleration to start sooner.

Equation (31) shows that the vapor pressure decreases when the initial vapor mass and density are reduced. Therefore, minimizing the initial vapor mass improves the areal densities at peak compression by increasing the shell convergence prior to the onset of the deceleration. The lower limit of the vapor pressure (when

the initial vapor mass is very small) is determined by the density rarefaction formed at the inner part of the shell during the implosion. A low-density tail of the released material travels ahead of the higher-density part of the shell, contributing to the vapor mass. A simplified scaling for the vapor mass with the implosion parameters can be obtained by assuming that a strong shock with a pressure p_{a} breaks out of a material with the post-shock sound speed c_{sa} and density ρ_{a} into the material with density $\rho_{\mathrm{v},0}$. The released material moves inward with the velocity[39]

$$v_{\mathrm{tail}} = v_{\mathrm{shell}} + 3c_{\mathrm{sa}} \left[1 - \left(\frac{p_{\mathrm{v,shk}}}{p_{\mathrm{a}}} \right)^{1/5} \right], \qquad (32)$$

where $p_{\mathrm{v,shk}}$ is calculated using Eq. (29). The accumulated mass in the rarefaction tail calculated from the lowest-density point up to the density ρ is

$$m_{\mathrm{rf}}(\rho) \simeq 4\pi R^2 c_{\mathrm{sa}} \rho_{\mathrm{a}} t \left[\left(\frac{\rho}{\rho_{\mathrm{a}}} \right)^{4/3} - \left(\frac{p_{\mathrm{v,shk}}}{p_{\mathrm{a}}} \right)^{4/5} \right], \qquad (33)$$

where R is shell position and t is time. Since the tail expands with a velocity greater than the shell's velocity [see Eq. (32)], the accumulated mass in the rarefaction increases with time, as shown in Eq. (33). Using the total shell acceleration time $t = t_{\mathrm{imp}} \sim E_{\mathrm{L}}/(4\pi R^2 I)$ (where E_{L} is the laser energy and I is the laser intensity) in Eq. (33) and writing the mass density as $\rho_{\mathrm{a}} \sim (p_{\mathrm{a}}/\alpha_{\mathrm{inner}})^{3/5}$ gives the scaling for the mass in the rarefaction tail at the end of the shell acceleration:

$$m_{\mathrm{rf}} \sim \left(\frac{E_{\mathrm{L}}}{I} \right) \alpha_{\mathrm{inner}}^{-3/10} p_{\mathrm{a}}^{4/5} C_\rho,$$

$$(34)$$

$$C_\rho = \left(\frac{\rho}{\rho_{\mathrm{a}}} \right)^{4/3} - \left(\frac{p_{\mathrm{v,shk}}}{p_{\mathrm{a}}} \right)^{4/5},$$

where α_{inner} is the adiabat of the inner part of the shell. Then, the contribution to the vapor pressure caused by the mass buildup from the rarefaction tail (the second contribution to the vapor pressure in our notation)

$$p_{\mathrm{v},2} = \mu \alpha_{\mathrm{inner}} \left(\frac{m_{\mathrm{rf}}}{V_{\mathrm{v}}} \right)^{5/3} \qquad (35)$$

with the help of Eq. (34) and the scaling for the initial vapor size [see Eq. (71) later in the text] becomes

$$p_{v,2} \sim C_\rho^{5/3} \sqrt{\alpha_{inner}} \frac{p_a^{4/3}}{v_{imp}^{5/3}} \left(\frac{V_{v,0}}{V_v}\right)^{5/3} . \qquad (36)$$

Matching Eq. (36) with the simulation results leads to using $\rho/\rho_a \sim 0.1$ in the coefficient C_ρ. As the fill pressure (vapor density) increases, $p_{v,shk}/p_a$ increases as well and the contribution to the hot-spot pressure from the material release into the target center becomes small. Equation (36) tends to overestimate the pressure because Eqs. (32) and (33) are written in the shell's frame of reference, assuming that v_{shell} is a constant in time. The shell velocity in ICF implosions, however, increases with time, reducing the velocity difference between the shell and the trailing edge of the rarefaction wave. This makes the mass in the rarefaction tail smaller than predicted by Eq. (34).

Since the rarefaction's contribution to the vapor pressure depends on the adiabat α_{inner}, material heating at the inner part of the shell caused by the shock mistiming, radiation, or suprathermal-electron preheat can result in a greater material expansion. In addition, significant reduction in the hot-spot pressure can occur compared to the case when such heating is not taken into account. In an optimized design, the gain in mass of the vapor region from the release is minimized by accurately timing shocks emerging from the cold fuel shell.

The third contribution to the pressure and the mass enhancement in the vapor region is due to multidimensional effects. These include jets of material created by local shell nonuniformities as well as fluxes of the ablated plasma through the holes in the shell that result from the excessive RT growth at the ablation front. These effects lead to an injection of the material with relatively high adiabat $\alpha_{mix} \gg \alpha_{shell}$ (Ref. 40). The vapor pressure contribution caused by the mix is

$$p_{v,3} = \mu \alpha_{mix} \left(\frac{m_{mix}}{V_v}\right)^{5/3} , \qquad (37)$$

where m_{mix} is the injected mix mass.

The effect of shell breakup and the ablator mass injection into the vapor region was studied in Ref. 40, where a series of 2-D *DRACO* simulations were performed assuming localized mass perturbations of 5 to 30 μm in diameter and 0.5 to 1 μm in height as an initial nonuniformity source on the outside of the target. The simulations show that these features significantly distort the first shocks launched by the intensity pickets early in the laser pulse, introducing significant modulations in

the lateral mass flow and creating low-density bubbles inside the ablator and the main fuel layer at the beginning of shell acceleration. Since the ablation stabilization is not efficient inside the cold bubbles,[41] the bubble growth is significantly enhanced as the shell starts to accelerate. The bubble velocity[42] $v_{bubble} \sim \sqrt{d_{bubble}g}$ (where d_{bubble} is the bubble diameter and g is the shell acceleration) competes with the material release rate at the inner surface of the shell [see Eq. (34)] and shell thickening resulting from convergence. When the bubble amplitude exceeds the in-flight shell thickness, the bubble "bursts" into the vapor region, injecting the ablator and the cold fuel mass into the central part of the target. In addition, the pressure difference between the ablation front and the vapor region creates a flow of ablated material from the plasma corona into the vapor region. Since the material releases more slowly in lower-adiabat shells and the main shell is thinner, the shells in such implosions are more likely to break up because of the bubble growth.

The simulation results, summarized in Fig. 9 of Ref. 40, indicate that to reduce the peak areal density by a factor of 2, the ablator and cold fuel material must be injected with a mass that is $\sim 15\times$ larger than the initial vapor mass. For the DT vapor at the triple point, the initial mass density is ~ 0.6 mg/cm^3, which corresponds to the initial vapor mass of 0.12 μg for OMEGA cryogenic targets.

Next, the inferred hot-spot pressure and the measured neutron-production rate in an $\alpha \sim 2$ cryogenic implosion are compared with the results of *DRACO* simulations. The level of the pre-imposed local defects in such simulations was varied to match the observed areal density and neutron yield. This leads to 2 μg of ablator and main fuel material being injected into the vapor region because of hydrodynamic instability growth during acceleration. The simulation results and the data are compared in Fig. 137.31. Observe the excellent agreement between simulation results and the data. This suggests that, indeed, the degradation in the performance of the low-adiabat implosions results from a significant mixing of the ablator material into the vapor region. The main source of the localized nonuniformities in OMEGA cryogenic targets, however, remains unknown. Significant shock distortions can be caused by either surface features or ice defects localized at the CD/DT interface created, for example, as a result of the early-time laser shinethrough.[43]

In summary, the pressure buildup inside the converging target is caused by compression of the original vapor mass, the material release from the inner part of the shell during accelera-
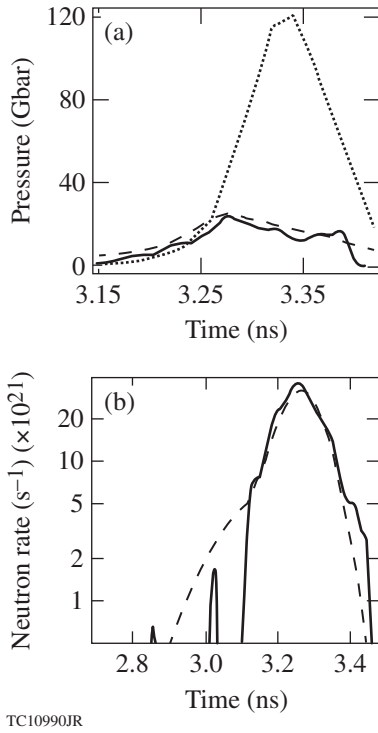
Figure 137.31

(a) The hot-spot pressure evolution inferred from the measurements (shot 66613, $\alpha = 2$) using Eq. (22) (solid line) and predicted using *LILAC* (dotted line) and *DRACO* (dashed line). (b) The neutron-production history measured (solid line) and predicted (dashed line) using *DRACO* simulations with the pre-imposed local defects on the outer surface of the target.

tion, and mixing of the ablator and cold fuel inside the target's vapor region because of the RT growth at the ablation front. The central pressure increase causes the early shell deceleration and stagnation, resulting in lower final fuel compression.

b. Shell acceleration and shell-pressure evolution. The onset of the shell deceleration depends not only on the vapor but also on the shell pressures because the shell begins to slow down when the radial pressure gradient pointing toward the target center is formed. During the early stages of an implosion, when the convergence effects are not important, the maximum shell pressure is equal to the ablation pressure and the pressure peak is localized near the ablation front. When convergence becomes important, the pressure maximum exceeds the ablation pressure and the pressure peak moves inside the shell. The basic features of the shell dynamics in convergent geometry can be studied using a model based on an approximate solution of the momentum–conservation equation. This model is described in **Appendix A**, p. 43, where the shell pressure is written as a second-order polynomial in the mass coordinate:

$$p(m,t) = p_a \left[1 + \hat{p}_1(t)\left(1 - \frac{m}{M}\right) + \hat{p}_2(t)\left(1 - \frac{m}{M}\right)^2 \right], \quad (38)$$

where m is the mass coordinate defined by a differential equation $dm/dr = 4\pi\rho r^2$ and M is the shell mass. The maximum shell pressure p_{shell} equals the ablation pressure p_a when $\hat{p}_1 < 0$; p_{shell} exceeds p_a when $\hat{p}_1$ becomes positive because of convergence effects [see Eq. (A2) for the dependence of $\hat{p}_1$ on the implosion parameters]. In the latter case, the peak pressure moves inside the shell and, consequently, the ablation front stops accelerating [see Eq. (A9)]. The time at which the pressure gradient at the ablation front changes from a positive to a negative value plays an important role in designing a target because this is when the absorbed laser energy no longer contributes to the shell's acceleration. Therefore, in an optimized implosion, the end of the laser drive must occur when $\hat{p}_1 \simeq 0$.

The ablation-front position at this time can be calculated with the help of Eq. (A13):

$$R_a \simeq R_0 \left[\frac{\epsilon}{3} \frac{M\dot{R}_a^2/2}{4\pi R_0^3 p_{a,0}}(2 - 3/5\beta)(1 - \beta/5) \right]^{1/(6 - 8/5\beta)}, \quad (39)$$

where R_a is the ablation-front radius and $p_{a,0}$ is the ablation pressure at the beginning of the shell's acceleration. The power index of the ablation-pressure evolution β and parameter ϵ are defined in Eqs. (A5) and (A7), respectively. Equation (39) can be rewritten as

$$\frac{M}{\rho_a V_a} \times \frac{M\dot{R}_a^2/2}{(3/2)p_a V_a} = \frac{1}{(1 - 3\beta/10)(1 - \beta/5)} \sim 1, \quad (40)$$

where $V_a = (4\pi/3)R_a^3$ is the target volume and ρ_a is the shell density at the ablation front (peak shell density). The first term in the left-hand side of Eq. (40) is proportional to the ratio of the shell's thickness to the ablation-front radius (this ratio is inversely proportional to the IFAR). The second term is the ratio of the shell's kinetic energy E_k and the internal energy $E_{in,a} = (3/2)p_a V_a$. The IFAR decays and the ratio of energies increases as the shell converges and accelerates. Therefore, the ablation front stops being accelerated when

$$\text{IFAR} \sim \frac{E_k}{E_{in,a}}. \quad (41)$$

The shell's kinetic energy and the ablation pressure do not depend on the shell adiabat, and, for a given shell radius, the IFAR is larger when the shell adiabat is lower. According to Eq. (41), compared to the higher adiabat, the lower-adiabat shells accelerate for longer distances.

Equation (40) can also be written in terms of the ablation-front Mach number $|\dot{R}_a|/c_s$:

$$\rho_a V_a = M \frac{|\dot{R}_a|}{c_s} \sqrt{\left(\frac{1}{3} - \frac{\beta}{10}\right)\left(\frac{5}{3} - \frac{\beta}{3}\right)}, \quad (42)$$

where $c_s = \sqrt{(5/3)(p_a/\rho_a)}$ is the shell's sound speed. The numerical factor in Eq. (42) varies from 0.45 to 0.65 for values of β relevant to the ICF implosions. During the implosion, the shell's density times the target volume $\rho_a V_a$ decreases (mainly because of a reduction in volume) and the shell's Mach number increases (because of an increase in $|\dot{R}_a|$). The ablation pressure stops accelerating the ablation front when these two terms are equal: $\rho_a V_a \sim M |\dot{R}_a|/c_s$. Even though the ablation-front velocity does not increase after that time, the parts of the shell where the pressure gradient is positive are still being accelerated. The total shell kinetic energy, therefore, keeps increasing until the vapor pressure exceeds the shell's pressure and a return shock is launched into the incoming shell. The longer the time delay between the end of the ablation-front acceleration and the return shock formation, the larger the velocity gradient in the shell and the lower the shell density, which results in lower stagnation pressures (for more details, see the discussion in **Shell Deceleration** below). Furthermore, the longer acceleration distances in the lower-adiabat implosions lead to enhanced RT growth factors at the ablation front. Note that the onset of ablation-front deceleration can be measured experimentally by imaging the x-ray emission from the plasma corona, as discussed in **Target Designs and Validation of 1-D Implosion Parameters**, p. 19.

After the location of the peak pressure moves from the ablation front inside the shell (because of the convergence effects), the shell mass coordinate of this location and the value of the peak pressure become

$$m_p = M\left(1 - \frac{1 + \hat{p}_2}{2\hat{p}_2}\right), \quad (43)$$

$$p_{shell} = -p_a \frac{(1 - \hat{p}_2)^2}{4\hat{p}_2}, \quad (44)$$

respectively. Note that p_{shell} is positive because $\hat{p}_2$ is negative. At this stage in the implosion, $\hat{p}_2$ can be simplified to

$$\hat{p}_2 \simeq -\frac{M\dot{R}_a^2/2}{3/2\rho_a V_a} \frac{C_\beta}{1 + 6/(4 - 3/5\beta)\rho_a V_a/M}, \quad (45)$$

where the coefficient $C_\beta = (2 - 3/5\beta)(3 - 3/5\beta)/(4 - 3/5\beta) \simeq 1$ changes from 0.8 to 1.2 for the values of β relevant to the direct-drive implosions.

In summary, the start of shell deceleration is determined by the relative evolutions of the vapor [Eqs. (31), (36), and (37)] and the shell [Eq. (44)] pressures. The target performance increases when the onset of deceleration is delayed. This is achieved by maximizing the shell and ablation pressures and minimizing the vapor pressure. The ablation front stops accelerating when $\rho_a V_a/M \sim |\dot{R}_a|/c_s$. The early ablation-front deceleration in the shells with higher adiabats, larger masses, and lower ablation-front densities leads to larger shell-velocity gradients and lower shell densities during the shell deceleration, resulting in lower stagnation pressures.

c. Shell deceleration. Soon after the vapor pressure exceeds the shell pressure [see Fig. 137.15(a)], a shock is formed at the inner surface of the shell, as illustrated in Fig. 137.32. The shock travels from the vapor region toward the ablation front. The inner part of the shell overtaken by the return shock (the shocked shell) is being decelerated by a force that is a
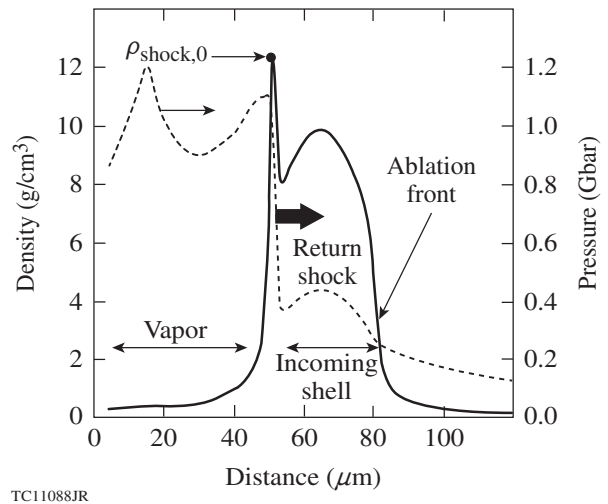

TC11088JR

Figure 137.32
The density (solid line, left axis) and pressure (dashed line, right axis) profiles at the time when the return shock is launched into the incoming shell.

consequence of the higher pressure at the hot spot p_{hs} and the lower pressure at the shock front p_{shock} (see Fig. 137.33). The hot-spot pressure continues to increase while the shocked shell converges inward, reducing the hot-spot volume (if the multi-dimensional effects are taken into account, the volume history depends also on the hot-spot distortion growth).
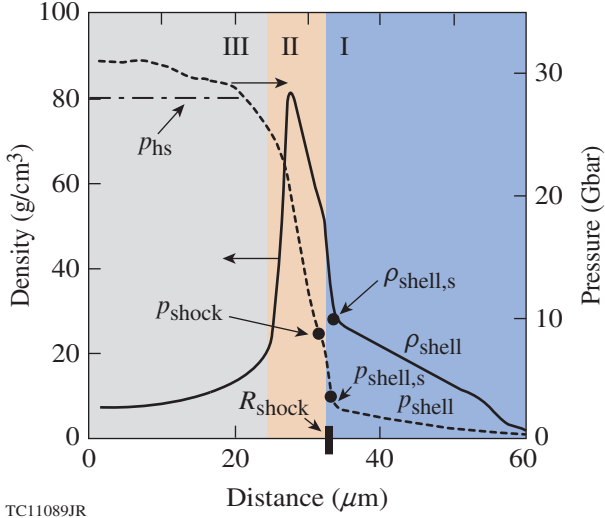

TC11089JR

Figure 137.33
Snapshots of the density (solid line, left axis) and pressure (dashed line, right axis) profiles during shell deceleration. The following three regions can be identified at this time: (I) the unshocked shell, (II) the shocked shell, and (III) the vapor region (hot spot).

The model describing the shell and hot-spot evolutions during the shell deceleration is presented in **Appendix B** (p. 45). Here, the main results are summarized.

The hot-spot radius R_{hs} is determined by the momentum–conservation equation (Newton's law)

$$\ddot{R}_{hs} = S_{hs} \frac{p_{hs} - p_{shock}}{M_s} \left(1 - \frac{M_s}{6\rho_{shock,0} V_{hs,0}} \right)^{-1}, \quad (46)$$

where S_{hs} is the surface area of the hot spot, $\rho_{shock,0}$ and $V_{hs,0}$ are the shell's density at the inner edge of the shell and hot-spot volume at the beginning of shell deceleration, respectively (see Fig. 137.32), and M_s is the mass of the shocked shell (shocked mass). The factor inside the brackets in Eq. (46) is due to the nonlinear variation of the shell's pressure with the mass coordinate. The shocked mass, shock pressure, and shock position are determined by Hugoniot conditions:[39]

$$\frac{dM_s}{dt} = \sqrt{\frac{\rho_{shell,s}}{3}} \sqrt{4p_{shock} + p_{shell,s}}\, S_{shock}, \quad (47)$$

$$p_{shock} = p_{shell,s} - \sqrt{\frac{\rho_{shell,s}}{3}\left(4p_{shock,s} + p_{shell,s}\right)}$$

$$\times \left(v_{shell,s} - v_{shock} \right), \quad (48)$$

and

$$\frac{dR_{shock}}{dt} = \sqrt{\frac{4p_{shock} + p_{shell,s}}{3\rho_{shell,s}}} + v_{shell,s}, \quad (49)$$

where S_{shock} is the shock-front area. Refer to Fig. 137.33 for definitions of $\rho_{shell,s}$, $v_{shell,s}$, and v_{shock}. In the strong-shock approximation, these relations are reduced to the expressions shown in Eq. (B9).

The shock pressure p_{shock} increases during the deceleration because of an increase in ρ_{shell} (resulting from the shell convergence) and the deceleration of the shocked shell (which leads to a reduction in $|v_{shock}|$). The rate of increase in p_{shock} is reduced by the deceleration of the unshocked shell (which leads to a reduction in $|v_{shock}|$).

Because of convergence, the density of the unshocked shell increases as

$$\rho(m,t) \simeq \rho_0(m)\left[\frac{r_0(m)}{r(m,t)}\right]^2$$

$$\times \left[1 + 4\pi C_d \frac{c_{s,0}}{M}(t - t_d)\rho_0(m)r_0(m)^2\right]^{-1}, \quad (50)$$

where the numerical coefficient $C_d = \sqrt{2(2 - 3/5\beta)/5 - \beta}$ ranges from 0.8 to 0.9 for the values of β relevant to the direct-drive implosions, $c_{s,0}$ is the shell's sound speed at the beginning of deceleration, $\rho_0(m)$ and $r_0(m)$ are the shell density and position as functions of mass coordinate at the beginning of shell deceleration, and t_d is the starting time of the shell deceleration. The deviation from a $1/r^2$ dependence in the density evolution is due to the velocity gradient inside the unshocked shell.

The reduction in the shocked shell velocity v_{shock} is calculated by relating it to the convergence rate of the hot spot,

$$v_{\text{shock}} = \dot{R}_{\text{hs}}\left(1 + \frac{M_s}{3\rho_{\text{shock},0}V_{\text{hs},0}}\right). \tag{51}$$

The velocity slowdown in the unshocked region is calculated using the momentum conservation $\mathrm{d}v_{\text{shell}}/\mathrm{d}t \sim -S_{\text{shock}}\,\partial p/\partial m$, where the pressure gradient is

$$\frac{\partial p}{\partial m} \simeq \left(\frac{r_0}{r}\right)^{10/3}\Sigma^{-8/3}\left[\frac{\partial p_0}{\partial m} + \frac{5p_0}{6\pi\rho_0 r_0^3}\right]$$

$$- \left(\frac{r_0}{r}\right)^{13/3}\Sigma^{-2/3}\frac{5p_0}{6\pi\rho_0 r_0^3}, \tag{52}$$

and

$$\Sigma = 1 + 4\pi C_d \frac{c_{s,0}}{M}(t - t_d)\rho_0(m)r_0(m)^2. $$

The second term in Eq. (52) grows faster than the first term. This leads to a negative pressure gradient and deceleration of the unshocked shell.

Equations (46)–(51), together with the hot-spot pressure's dependence on shell convergence [see Eq. (24)], define the deceleration model. It can be used to study the effects of different implosion parameters on the peak hot-spot pressure. Using these equations, simplified scalings for the hot-spot pressure and shocked mass are derived in **Implosion Scaling Laws** (below) to guide a physical understanding of deceleration dynamics.

In summary, the maximum hot-spot pressure depends on the convergence ratio of the shocked shell, which, in turn, depends on the shell's deceleration rate. The larger the pressure gradient inside the shocked shell (larger difference between p_{hs} and p_{shock}) and the smaller the rate of increase in the shocked mass $(\mathrm{d}M_s/\mathrm{d}t)$, the larger the shell deceleration rate and the smaller the final convergence ratio of the shell. The pressure gradient increases and the rate of the shocked mass growth is reduced if the density and velocity of the incoming shell are reduced. The pressure gradient is also increased in implosions with a larger vapor mass and pressure at the onset of shell deceleration.

Discussion

This section derives the simplified scaling laws for the hot-spot pressure and the shocked mass at stagnation. Then, to quantify the effects of the ablation-front mix and the ablator-

to-vapor mix on target performance, the measured areal density is shown as a function of the predicted unshocked-shell mass.

1. Implosion Scaling Laws

The model described in the previous section suggests the following simplified description of shell deceleration and hot-spot formation: The hot-spot pressure continues to increase until the shell's material overtaken by the return shock stagnates. If the duration of shell deceleration is Δt_{dec}, Eq. (46) gives

$$\frac{v_{\text{imp}}}{\Delta t_{\text{dec}}} \sim S_{\text{hs}}\left(p_{\text{hs}} - p_{\text{shock}}\right)\big/M_s. \tag{53}$$

The shell mass overtaken by the shock (the shocked mass), according to Eq. (B9), is

$$\frac{M_s}{\Delta t_{\text{dec}}} \sim \frac{p_{\text{shock}}}{v_{\text{imp}}}S_{\text{shock}}. \tag{54}$$

Eliminating the mass M_s and the time Δt_{dec} from Eqs. (53) and (54) yields a relation between the hot-spot and shock pressures:

$$p_{\text{hs}} \sim p_{\text{shock}}\left(1 + S_{\text{shock}}\big/S_{\text{hs}}\right) \simeq 2p_{\text{shock}} \sim \rho_{\text{shell}}v_{\text{imp}}^2. \tag{55}$$

Neglecting the velocity gradient inside the unshocked shell, the density increase caused by the shell's convergence becomes [see Eq. (50)]

$$\rho_{\text{shell}} \sim \rho_{\text{shell},0}\left(\frac{R_{\text{hs},0}}{R_{\text{hs}}}\right)^2, \tag{56}$$

and the hot-spot pressure scales with the convergence ratio as [see Eq. (25)]

$$p_{\text{hs}} = p_{\text{hs},0}\left(\frac{R_{\text{hs},0}}{R_{\text{hs}}}\right)^5. \tag{57}$$

Eliminating p_{hs} from Eqs. (55) and (57) gives the hot-spot convergence ratio

$$\frac{R_{\text{hs},0}}{R_{\text{hs}}} \sim \left(\frac{\rho_{\text{shell},0}v_{\text{imp}}^2}{p_{\text{hs},0}}\right)^{1/3}. \tag{58}$$

Equation (58) shows that having a larger vapor pressure (because of a larger initial vapor mass, higher shell adiabat, or ablator-to-vapor mix) at the start of shell deceleration leads to a lower hot-spot convergence ratio and a smaller peak pressure.

Combining Eq. (58) with Eq. (25) gives a scaling for the hot-spot pressure:

$$p_{hs} \sim p_{hs,0} \left(\frac{\rho_{shell,0} v_{imp}^2}{p_{hs,0}} \right)^{5/3} = \left(\rho_{shell,0} v_{imp}^2 \right)^{5/3} p_{hs,0}^{-2/3} . \quad (59)$$

Similar to Eq. (58), Eq. (59) also demonstrates the benefit of reducing the vapor pressure $p_{hs,0}$ at the start of shell deceleration. Since the vapor pressure at that time equals the shell's pressure (which scales as the ablation pressure p_a), $p_{hs,0} = p_{shell,0} \sim p_a$, $p_{shell,0} \sim \alpha_{shell} \rho_{shell,0}^{5/3}$, and the scaling for the maximum pressure reduces to

$$p_{hs} \sim \frac{p_a^{1/3} v_{imp}^{10/3}}{\alpha_{shell}} . \quad (60)$$

Using Eq. (60) in Eq. (2) leads to a scaling for the minimum shell kinetic energy required for ignition,

$$E_{k,min} \sim v_{imp}^{-20/3} p_a^{-2/3} \alpha_{shell}^2 . \quad (61)$$

This scaling is similar to that obtained using simulation results.[44]

Because of its limited region of validity, the scaling law given in Eq. (60) should be used mainly as a guiding tool in understanding the effects of different implosion parameters on the shell's properties at peak compression. The limitations in applicability of Eq. (60) include the following: According to Eq. (50), the shell density's dependence on the convergence ratio is somewhat weaker than that shown in Eq. (56). This leads to a smaller power index in the velocity dependence than shown in Eq. (60).

Second, as the implosion velocity increases or the shell adiabat decreases, Eq. (60) becomes invalid since the shocked mass predicted by Eq. (54) exceeds the total shell mass. To clarify the latter statement, the shocked mass is estimated by using the energy-conservation equation. The kinetic energy of the shocked shell $M_s v_{imp}^2 / 2$ is converted into the internal energy of the hot spot $3/2\, p_{hs} V_{hs}$ and the shocked shell $E_{shell} = 3/2 \int p dV$. The latter term is estimated by using the expression for the pressure profile as shown in Eq. (B1):

$$E_{shell} = 3/2\, M \int_0^{M_s/M} \frac{p(m')}{\rho(m')} dm' , \quad (62)$$

where $m' = m/M$ is the normalized mass coordinate, $\rho = (p/\mu \alpha_{shock})^{3/5}$, and α_{shock} is the adiabat of the shocked shell. It can be shown that the integral in Eq. (62) scales as $E_{shell} \sim M_s v_{imp}^2$. As a result, energy conservation leads to

$$M_s v_{imp}^2 \sim p_{hs} V_{hs} , \quad (63)$$

which, in combination with Eq. (55), gives

$$M_s \sim \rho_{shell} V_{hs} . \quad (64)$$

Substituting the scalings for the shell's density and the hot-spot volume from Eqs. (56) and (58) gives

$$M_s \sim \frac{p_a^{11/15} R_{hs,0}^3}{\alpha^{2/5} v_{imp}^{2/3}} . \quad (65)$$

The scaling for the shocked mass must be compared with the scaling for the total shell mass. The latter is derived by combining the relations between the initial shell radius and the implosion velocity, $R \sim v_{imp} t_{imp}$, and the shell mass and the ablation pressure (Newton's law), $M v_{imp} / t_{imp} \sim R^2 p_a$. The implosion time can be written as the ratio of the laser energy and laser power, $t_{imp} \sim E_{laser} / R^2 I$, where I is the laser intensity. This gives

$$M \sim \frac{p_a E_{laser}}{v_{imp} I} , \quad R \sim \left(\frac{E_{laser} v_{imp}}{I} \right)^{1/3} . \quad (66)$$

Substituting Eq. (66) into Eq. (65) and assuming that the scalings of $R_{hs,0}$ and the initial shell radius R are the same yield,

$$\frac{M_s}{M} \sim \frac{v_{imp}^{4/3}}{\alpha^{2/5} p_a^{4/15}} , \quad M_s \sim \frac{p_a^{11/15} v_{imp}^{1/3}}{\alpha^{2/5}} \frac{E_{laser}}{I} . \quad (67)$$

To increase v_{imp} for a given laser energy and intensity, the shell mass, according to Eq. (66), must be reduced. The shocked mass, however, increases with v_{imp} [see Eq. (67)]. Consequently, as v_{imp} keeps increasing, Eq. (67) becomes invalid at some point when M_s exceeds M. This defines the validity region for the scaling laws shown in Eqs. (67) and (60).

2. Relating Target Performance to the Unshocked Mass

In optimizing the target performance, there is a trade-off between maximizing 1-D performance and controlling the hydrodynamic instabilities. Indeed, the larger the fraction of the shell overtaken by the return shock at the hot-spot stagnation, the larger the fraction of the shell's kinetic energy being converted into the hot-spot internal energy. Equation (67) shows that increasing the implosion velocity and reducing the shell's adiabat results in a larger shocked mass and, according to Eq. (60), a higher hot-spot pressure.

The lower-adiabat shells, however, are more susceptible to the RT growth during the acceleration because of reduced ablative stabilization. The larger instability growth leads to a larger region of relaxed density at the outer part of the shell. As the outgoing shock travels through such a lower-density mix region during shell deceleration, the shock pressure $p_{\text{shock}} \sim \rho_{\text{shell}} v_{\text{imp}}^2$ is reduced and the shell's deceleration rate increases [see Eq. (53)]. The stronger deceleration force stops the shell while the hot spot is at a larger radius, leading to a reduction in the hot-spot pressure. This also follows from Eq. (59), which shows that $p_{\text{hs}} \sim \rho_{\text{shell}}^{5/3}$.

Degradation of the target performance depends on the mass (or size) of the mix region that contributes to the shocked mass at stagnation. If the hot spot stagnates before the return shock reaches the mix zone, the effect of the RT growth is small, as illustrated in Fig. 137.34. Vice versa, if the shocked mass at stagnation includes a significant fraction of the mixed mass, the hot-spot convergence and peak pressure are reduced. This
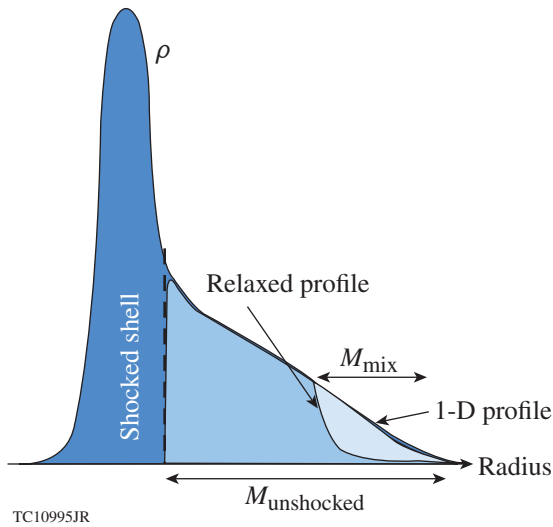
is illustrated in Fig. 137.35, which plots the results of a series of *LILAC* simulations of cryogenic implosions where the shell's density was artificially relaxed (without changing the shell velocity or mass) at the beginning of shell deceleration. A reduction in the hot-spot pressure in these simulations depends on the fraction of relaxed material in the shocked mass at peak compression. In the case where the mix region extends to include 60% of the shocked mass (as calculated in the no-mix run), the peak areal density is reduced by 50% and the peak pressure by 60% compared to the results of the no-mix simulation.
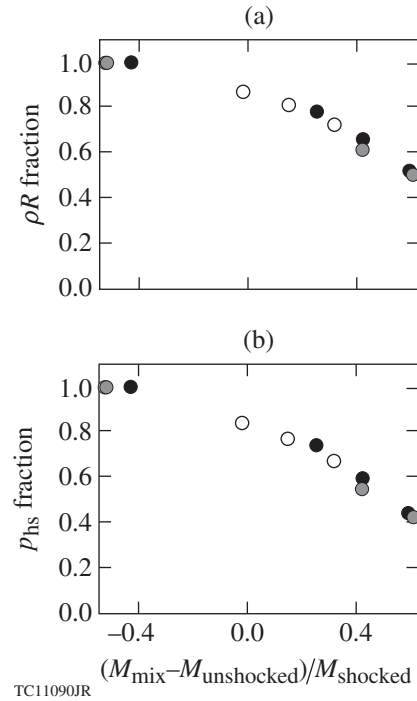

TC11090JR

Figure 137.35
LILAC predictions of (a) the areal density and (b) the peak hot-spot pressure fractions as functions of the relaxed shell fraction in the shocked mass at peak compression. Different symbols indicate different target designs.

To quantify the effects of hydrodynamic instability growth on target performance, the measured areal-density reduction relative to 1-D predictions is plotted as a function of the calculated unshocked mass at bang time. Figure 137.36 shows the experimental areal-density (normalized to *LILAC* predictions) contours in the shell adiabat/unshocked mass parameter space. A stability boundary can be identified (plotted with a thick solid line) that separates the region where more than 85% of the predicted areal density is measured and the region of reduced areal densities, where the effect of the instability growth is significant.

TC10995JR

Figure 137.34
An illustration of the shell density at peak compression.
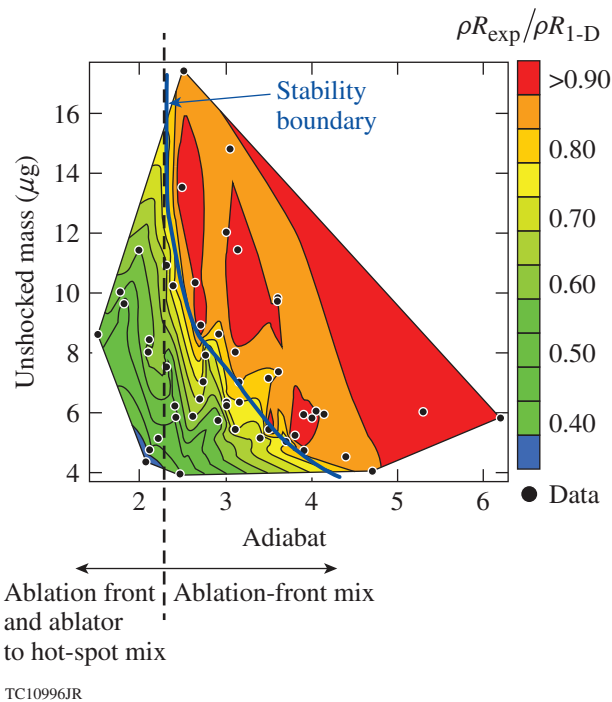
Figure 137.36
Contour map of the measured areal-density reduction relative to 1-D predictions. The unshocked mass is calculated at bang time using *LILAC*. The vertical dashed line separates the parameter space into a region (on the right from the line) where a line representing implosions with a fixed adiabat intersects with the stability boundary (thick solid line) and a region (on the left from the line) where the measured areal densities are below 70% of 1-D predictions for all values of the unshocked mass.

According to Fig. 137.36, the measured areal-density fraction, for a given shell adiabat, increases with the unshocked mass. The 1-D–predicted values are achieved, however, only if $\alpha > 2.3$. For these implosions, a vertical line representing a fixed adiabat always intersects with the stability boundary. The mass given by a point of intersection of the vertical line with the stability boundary represents the mass $M_{mix}\alpha$ of the mix region at the ablation front. A line with $\alpha = 3$, for example, intersects the stability boundary at $M_{mix}(3) = 8$ μg, indicating that the shell compression is not degraded if the unshocked mass is larger than M_{mix}. Then, according to Fig. 137.35, M_{mix} is equal to the mass of relaxed density at the ablation front (mix mass), and the stability boundary represents the points where the mix mass is equal to the shocked mass. The dependence of the mix mass on shell adiabat (the position of the stability boundary) is shown in Fig. 137.37.

For implosions with $\alpha < 2.3$ (the region to the left of the dashed vertical line in Fig. 137.36), a line of constant adiabat never intersects the stability boundary. This indicates that, in addition to the density relaxation at the ablation front, a
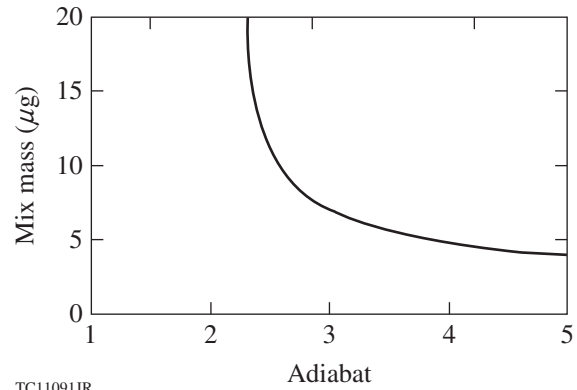

Figure 137.37
Mix mass M_{mix} as a function of shell adiabat. The mix mass equals the total shell mass for $\alpha < 2.3$ since these shells are broken during acceleration.

different performance degradation mechanism limits the target compression. A possible mechanism is suggested by the observed correlation between the measured x-ray emission and the shell adiabat. This is shown in Fig. 8 of Ref. 23, where the calculated and measured core x-ray emission in the sensitivity range of the gated x-ray imager (4 to 7 keV) and normalized to neutron yield to the power of 0.57 is plotted for different values of the shell adiabat. The enhanced x-ray emission from the target core is observed in the low-adiabat implosions with $\alpha < 2.3$ and can be explained by the presence of carbon in the hot spot at the peak of x-ray production. This is due to shell breakup and the CD ablator penetrating into the vapor region during the shell's acceleration. Breakup of the shell increases the vapor mass and reduces the shell's density. Both effects lead to an early shell deceleration and a significant reduction in the peak areal densities and hot-spot pressures. Because the CD layer in these implosions is totally ablated by the end of the drive pulse, the only mechanism that is capable of mixing the CD ablator into the vapor region is the nonlinear evolution of the localized surface defects (or ice features) at the early stages of the implosion.[40] The bubbles of the lower-density material break shell integrity at the beginning of the shell's acceleration, bringing the cold fuel, the ablator material, and the ablated plasma into the vapor region and compromising target performance. This result suggests that the bubble velocity $v_{bubble} \sim \sqrt{d_{bubble}g}$ (where g is the shell acceleration and d_{bubble} is the bubble diameter) in the implosions with $\alpha < 2.3$ exceeds the rate of increase in the in-flight shell thickness.

3. Toward Demonstration of the Ignition Hydrodynamic Equivalence in Cryogenic Implosions on OMEGA
 a. The hot-spot pressure requirement for an igniting target.
As shown in **Target Performance** (p. 23), cryogenic implosions

on OMEGA have reached maximum hot-spot pressures of up to ~40 Gbar. The pressure requirement for ignition demonstration on the NIF can be derived using Eq. (3), which, with the help of Eq. (24), reduces to

$$\left(\frac{p_{hs}}{100\,\text{Gbar}}\right)^{4/5}\left(\frac{p_{hs,0}}{100\,\text{Gbar}}\right)^{1/5} > \frac{100\,\mu m}{R_{hs,0}}. \qquad (68)$$

The size of the vapor region at the beginning of shell deceleration $R_{hs,0}$ is determined by equating the vapor and shell pressures. Assuming that the convergence of the original vapor mass has the largest contribution to $p_{hs,0}$ (see **Vapor Pressure Evolution**, p. 29), Eq. (31) is used to obtain

$$p_{hs,0} = p_{a,0} F\left(\frac{\rho_{v,0}}{\rho_{ice,0}}\right)\left(\frac{R_{v,0}}{R_{hs,0}}\right)^5, \qquad (69)$$

where $R_{v,0}$ is the initial (undriven) size of the vapor region, $\rho_{v,0}$ and $\rho_{ice,0}$ are the initial densities of the vapor and the main fuel, respectively, and the function $F(x)$ is defined as

$$F(x) = \frac{x}{4^{5/3}}\left[1 + 2\sqrt{5}\left(1 - x^{1/5}\right)\right]. \qquad (70)$$

At the DT triple point, $\rho_{v,0} \simeq 0.6\,\text{mg/cm}^3$ and $\rho_{ice,0} \simeq 0.25\,\text{g/cm}^3$, so $F \simeq 10^{-3}$. The initial vapor radius scales with the target radius. The latter is given in Eq. (65), which, including the numerical coefficients, takes the form

$$R_{v,0} \simeq 0.85\left(\frac{E_{laser}v_{imp}}{4\pi I}\right)^{1/3}. \qquad (71)$$

Combining Eqs. (68)–(71) leads to the following requirement for the minimum hot-spot pressure in an igniting target:

$$p_{hs} > 120\,\text{Gbar}\left(\frac{100\,\text{Mbar}}{P_{a,0}}\right)^{1/4} I_{15}^{5/12}\left(\frac{E_{laser}}{1.5\text{J}}\right)^{-5/12}$$

$$\times \left(\frac{v_{imp}}{3.7\times 10^7\,\text{cm/s}}\right)^{-5/12}, \qquad (72)$$

where I_{15} is the incident laser intensity in 10^{15} W/cm². Equation (72) shows that the cryogenic implosions, hydrodynami-

cally equivalent to an igniting target on the NIF, must achieve central pressures in excess of ~100 Gbar. Therefore, the maximum hot-spot pressures inferred in the cryogenic implosions on OMEGA are lower by a factor of 2 to 3 than what is required for ignition demonstration on the NIF.

According to Figs. 137.25 and 137.29, the reduction in the central pressure is larger than the reduction in areal density. More than 85% of the 1-D–predicted ρR values are observed in the implosions without significant ablator mixing into the vapor region or density relaxation at the ablation front. In contrast, the inferred central pressures in such implosions are reduced by more than 60%. This is a result of the hot-spot distortion growth during the shell's deceleration. When integrity of the in-flight shell is not compromised by the RT growth, a large fraction of predicted areal density is observed if the mix mass at the ablation front does not exceed the unshocked mass at bang time (see Fig. 137.36). Perturbations at the inner edge of the shell (seeded because of the feedthough from the ablation front) grow during the deceleration as a result of the RT instability since the pressure and density gradients have opposite signs at the inner surface of the shell. Such a growth leads to an increase in the hot-spot volume and the surface area. The larger surface area of the colder shell leads to enhanced thermal-conduction losses from the hotter central region and larger mass ablation from the shell into the hot spot. This reduces the hot-spot temperature and truncates the neutron production before the hot spot reaches its minimum volume. Since the hot-spot pressure is inferred from the nuclear-reaction products, the early burn truncation prevents sampling the pressures at higher hot-spot convergence ratios, thereby reducing the inferred pressure values.

The second multidimensional effect that leads to a reduction in the hot-spot pressure is the growth of the nonradial flow caused by the shell's distortion growth. This reduces the fraction of the shell's kinetic energy that is converted into hot-spot internal energy. In a spherically symmetric implosion, the full kinetic energy of the shocked shell, $1/2\,M_s v_{shell}^2$, is converted into the internal energy of the hot spot and shocked shell:

$$\frac{1}{2}M_s v_{shell}^2 \longrightarrow \frac{3}{2}p_{hs}V_{hs} \qquad (73)$$

(spherically symmetric implosion). In the presence of asymmetries, there is a residual fluid motion in the shocked region because of the RT growth. This leads to

$$\frac{1}{2}M_s v_{shell}^2 \longrightarrow \frac{3}{2}p_{hs}V_{hs} + \frac{1}{2}M_s v_{RT}^2 \qquad (74)$$

(asymmetric implosion) and a reduction in $p_{hs}V_{hs}$ compared to the symmetric implosion. In addition, only the velocity component normal to the shock front $v_{shell,\perp}$ contributes to the shock pressure shown in Eqs. (B7) and (55), so only a fraction of the incoming shell dynamic pressure is converted into shock pressure p_{shock}:

$$\frac{4}{3}\rho_{shell}v^2_{shell,\perp} \rightarrow p_{shock} \qquad (75)$$

(asymmetric implosion). This reduces the shock pressure and increases the pressure gradient inside the shocked shell, leading to a larger deceleration force, larger hot-spot volume, and smaller hot-spot pressure at peak compression.

    b. Direct-drive target designs with improved shell stability. Since the numerical simulations and the experimental data suggest that only ~40% of the 1-D–predicted peak pressures are observed in the presence of the perturbation growth, demonstrating the ignition hydrodynamic scaling on OMEGA with peak pressures of ~100 Gbar requires a 1-D design that reaches $p_{hs} \sim 200$ Gbar at stagnation. Such a design is shown in Fig. 137.38 (the pulse shape is plotted in red and the target is labeled "nominal CBET"). This design is driven at a peak laser intensity of 9.5×10^{14} W/cm^2 and reaches an implosion velocity

of 3.7×10^7 cm/s. The calculated unshocked mass, fuel adiabat, and in-flight aspect ratio are $m_{unshocked} = 6~\mu$g, $\alpha = 1.65$, and IFAR = 30, respectively. Figures 137.25(b) and 137.36 both show, however, that such a design is unstable, assuming the nonuniformity seeds currently present in OMEGA cryogenic implosions. Therefore, the shell's stability must be improved to demonstrate the hydrodynamic equivalence. This can be achieved by reducing the level of the nonuniformity seeds [which will move the stability boundary shown in Figs. 137.25(b) and 137.36 to a region with lower adiabat values, unshocked shell masses, and higher IFAR's] and by increasing the hydrodynamic efficiency of the imploding target. At higher hydrodynamic efficiency of the laser drive, the required peak hot-spot pressure can be reached in the implosions with the higher-adiabat values, unshocked masses, and lower IFAR's, moving the hydro-equivalent design into the stable region in the adiabat/IFAR and adiabat/unshocked mass parameter spaces.

    Identifying the dominant nonuniformity seed is currently underway at LLE. The possible sources include the target defects introduced during the fill, cooling, and layer formation, as well as the early laser shinethrough, and the first shock interaction with modulations in the solid-state properties of the ablator.

    Improving the shell's stability by raising its adiabat and IFAR (keeping the hot-spot pressure fixed) can be achieved [according to the scaling shown in Eq. (60)] by increasing the ablation pressure p_a. The main factor limiting the laser absorption and ablation pressure in direct-drive implosions is cross-beam energy transfer (CBET).[12] Therefore, the most-efficient mechanism in raising p_a is to mitigate the CBET. LLE is currently pursuing several mitigation approaches,[12,45] including reducing the laser-beam size relative to the target size, increasing the laser bandwidth, and introducing layers of mid-Z (Si, for example) materials inside the ablator. The benefit of CBET mitigation on target characteristics is illustrated in Fig. 137.38, where the designs with various fractions of laser-deposition reduction caused by CBET are shown. The maximum hot-spot pressure, shell velocity, and peak areal density in these designs are kept constant. The effect of CBET in simulations is varied by introducing a multiplication factor in front of the growth rate for the stimulated Brillouin scattering (SBS)[14] (the design labeled "1/2 CBET" is simulated using a factor of 1/2 in front of the SBS growth rate, and the simulation of the "no CBET" design shows no effect from CBET). Reducing CBET increases the ablation pressure, leading to a hydro-equivalent design with an increased fuel adiabat. The shell parameters for these designs are summarized in Table 137.V. The shell IFAR, fuel adiabat, and unshocked mass for the three designs are indicated in Fig. 137.39 by the solid circles. Also shown are the
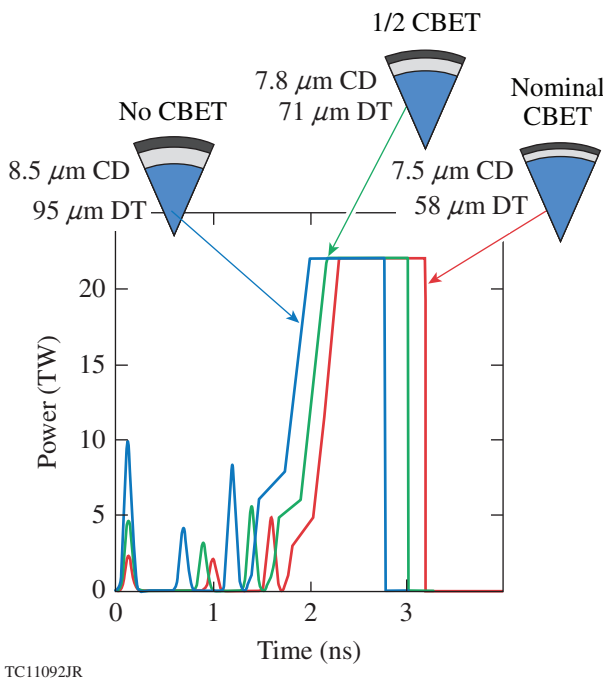

TC11092JR

Figure 137.38
OMEGA cryogenic target designs with 1-D central pressures of 180 Gbar at stagnation, the implosion velocity of 3×10^7 cm/s, and neutron-averaged areal density of 300 mg/cm^2.

Table 137.V: Summary of the shell parameters for the designs shown in Fig. 137.38. All designs have a peak hot-spot pressure of 180 Gbar, a neutron-averaged areal density of 300 mg/cm^2, and an implosion velocity of 3.7×10^7 cm/s.

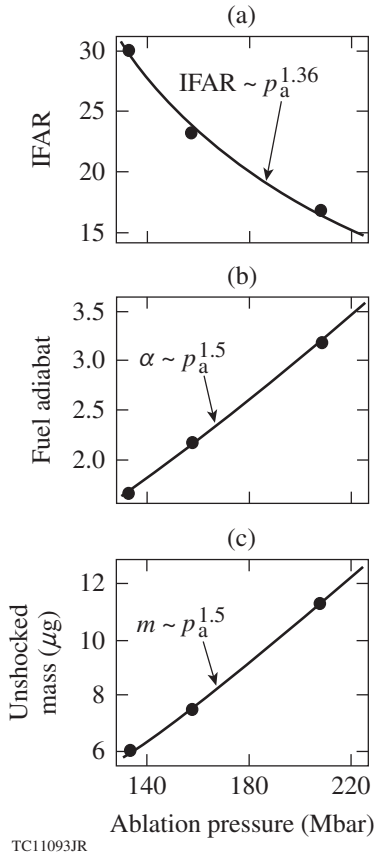| Parameters	Nominal CBET	1/2 CBET	No CBET
Ablation pressure (Mbar)	138	162	213
IFAR	30	23	17
In-flight adiabat	1.6	2.2	3.2
Unshocked mass (μg)	6.0	7.5	11.3
Total unablated shell mass (μg)	17.4	19.4	23.7
Initial shell mass (ablator and DT) (μg)	47.1	53.1	63.4

Figure 137.39
(a) Shell IFAR, (b) fuel adiabat, and (c) the unshocked mass at peak neutron production as functions of ablation pressure for the designs shown in Fig. 137.38. Solid lines represent the best fit to the simulation results. Solid circles show the simulation results.

best fits to the simulation data. The IFAR scales with the ablation pressure as IFAR $\sim p_a^{1.36}$, while the fuel adiabat and the unshocked mass scale as $p_a^{1.5}$.

<u>c. CBET mitigation strategies.</u> Different CBET mitigation strategies are compared by calculating the ablation pressure using the CBET model in *LILAC*.[12] As discussed in Refs. 12 and 45, reducing the beam size relative to the target size mitigates the effect of CBET. Figure 137.40 shows the predicted ablation pressure in OMEGA cryogenic implosions as a function of the ratio of the beam to the target radii. $R_{\text{beam}}/R_{\text{target}} \sim 0.8$ is equivalent to the 1/2 CBET design; reducing the beam radius to $R_{\text{beam}} \sim 0.6\, R_{\text{target}}$ leads to an ablation pressure similar to that of the no CBET design shown in Fig. 137.38. This does not mean, however, that CBET is completely suppressed at such a beam radius. Two effects cause an increase in the ablation pressure with a reduction in the beam size.[12] The first is a reduction in CBET; the second is a decrease in the average angle of incidence in the laser illumination. The beam rays, which have a smaller incident angle to the target surface, propagate farther toward the higher electron densities,[14] depositing their energy more efficiently. Consequently, a combination of CBET reduction and a decrease in the average angle of incidence in the illumination leads to matching the ablation pressure in the $R_{\text{beam}}/R_{\text{target}} \simeq 0.6$ design with a pressure when the CBET is fully mitigated at $R_{\text{beam}}/R_{\text{target}} \simeq 1$.

The smaller beams produce, however, an increased illumination asymmetry. Using the smaller beams at the beginning of the laser drive increases nonuniformity caused by the limited beam overlap. The reduced beam overlap also increases the sensitivity
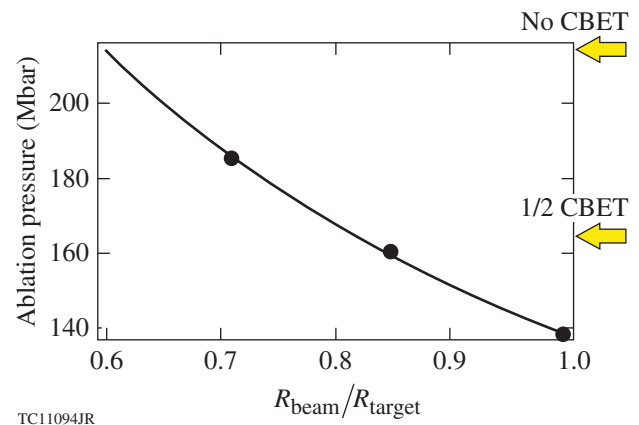

Figure 137.40
The ablation pressure as predicted by *LILAC* (including the CBET effect) versus the ratio of the beam to the target radii. Data points show the simulation results; the solid line is the best fit to the simulations.

of the target design to the power imbalance and beam mistiming. To mitigate the increased early-time overlap nonuniformity, a two-stage zooming scheme has been proposed,[45] where $R_{beam}/R_{target} \simeq 1$ is used until the onset of the main drive and $R_{beam}/R_{target} < 0.7$ is used thereafter. Controlling the single-beam uniformity for modes $20 < \ell < 100$ is the main challenge for this mitigation scheme. To optimize the target design, one must find a compromise between improving the target stability properties (reduced IFAR but increased adiabat and unshocked mass) and increasing illumination nonuniformity seeds (but keeping them at a tolerable level). Several zooming implementation options are currently being pursued on OMEGA.

Mitigating CBET by increasing the laser bandwidth[12] requires wavelength separation in excess of 5 Å at a laser wavelength of $\lambda = 351$ nm. The CBET model implemented in *LILAC* suggests[12] that this effectively reduces the SBS gain by a factor of 2, leading to the 1/2 CBET target design shown in Fig. 137.38. Currently, this is considered to be the best option in mitigating CBET in the polar-drive implosions on the NIF.
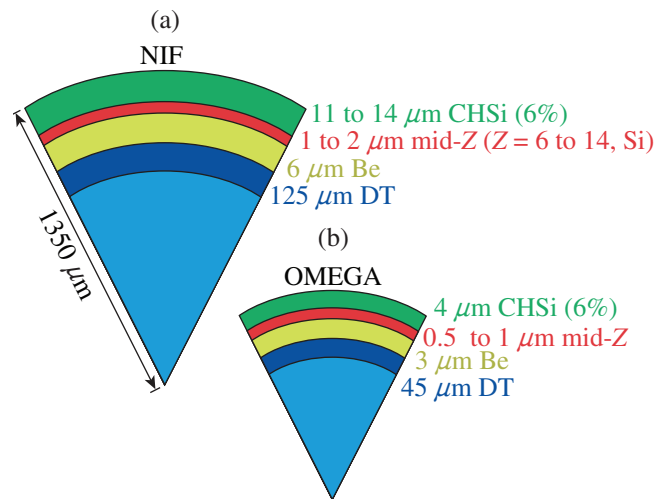
There are several beneficial effects from introducing a mid-Z layer inside the ablator: First, having a higher-Z material inside the laser-absorption region leads to increased inverse bremsstrahlung absorption, as discussed in **Target Designs and Validation of 1-D Implosion Parameters**, p. 19. Consequently, even if the laser-deposition reduction caused by CBET is held constant, the higher-Z ablators lead to higher absorption. This also increases the coronal temperature, which, in turn, reduces the SBS gain that governs the CBET.

An additional benefit in using a mid-Z layer is the mitigation of TPD instability. Again, as mentioned on p. 19 and discussed in detail in Ref. 16, the higher-Z plasma at quarter-critical surface reduces the ion-wave damping rate, leading to a reduction in TPD growth. An increase in the coronal temperature caused by the higher laser absorption is also beneficial for the mitigation of TPD instability.

The higher-Z materials have several disadvantages [such as low hydroefficiency, radiation losses, radiation preheat, etc. (see discussion on p. 19)] that diminish the benefits of the CBET reduction. To overcome these shortcomings, a relatively thin layer of a mid-Z material (such as Si) is introduced inside the lower-Z materials to combine the higher laser absorption with the larger ablation efficiency of the innermost layer in the ablator. DT has the highest ablation efficiency (because of the large ratio of atomic mass to the ion charge) but the lowest ion charge and, therefore, the smallest inverse bremsstrahlung

absorption. Having the mid-Z layer extended all the way to the DT layer causes either significant radiation preheat of the main fuel because of radiation from the plasma corona (if the layer is thick) or a significant loss in the laser absorption by depositing laser energy in the DT during the main pulse (if the layer is thin). Both reduce the benefits of having a higher ion charge in the plasma corona.

The best design option is to introduce an intermediate layer between the mid-Z layer and the DT ice. The material in this layer must have high ablation efficiency, while the ion charge must be larger than 1 to avoid significant losses in laser absorption. From a target-manufacturing point of view, beryllium is the best choice for such a purpose.[19] The hydro-equivalent "multi-layer" design for OMEGA and the ignition design for the NIF are shown in Fig. 137.41. The OMEGA multilayer cryogenic design is predicted to absorb 60% of the incident laser energy. This is compared with the 54% absorption achieved in the plastic-ablator designs. The higher absorption fraction results in an increase in the ablation pressure to 147 Mbar, fuel adiabat to $\alpha \simeq 2$, and the unshocked mass to 7 μg. These indicate a moderate improvement in the design parameters compared to the "nominal CBET" design shown in Table 137.V. The NIF multilayer design, shown in Fig. 137.41, is predicted to ignite in 1-D and produce a gain of 5 if no additional CBET mitigation strategies are used. Employing a laser wavelength separation of 5 Å in the UV further reduces CBET and increases the gain to 20. Additional strategies that will increase the shell's convergence and target gain are currently being considered at LLE.

(a)
NIF

11 to 14 μm CHSi (6%)
1 to 2 μm mid-Z (Z = 6 to 14, Si)
6 μm Be
125 μm DT

1350 μm

(b)
OMEGA

4 μm CHSi (6%)
0.5 to 1 μm mid-Z
3 μm Be
45 μm DT

TC10544JR

Figure 137.41

(a) Multilayer ignition design for the NIF and (b) hydro-equivalent design for OMEGA. The outer plastic layer is doped with Si to reduce laser imprint.[46]

Although much more work is required to validate the predicted benefits and access the stability properties of the multilayer design, the first experiments performed on OMEGA using the multilayer warm targets, where a cryogenic layer is replaced by an extra layer of Be, have confirmed an increased coronal temperature compared to that in implosions using the pure plastic shells.[47] The generation of suprathermal electrons caused by TPD instability is also observed to be reduced in the multilayer design.

Conclusions

The target performance of cryogenic implosions on OMEGA has been discussed. The implosion velocity was varied from 2.2 to 3.8×10^7 cm/s and the shell adiabat from 1.5 to 5. Based on the results of these experiments, the stability boundaries in the IFAR adiabat and unshocked mass-adiabat parameter spaces were identified. These show that the target designs operating above the boundary achieve more than 85% of the 1-D–predicted areal densities. The hot-spot pressures and yields are up to 35% and 40% of the predictions, respectively. The target performance of the implosions in this stability regime is well understood using *DRACO* simulations.

A measure of the effect that ablative RT growth has on target performance is the fraction of the mix-region mass in the shocked mass. If the return shock has not reached the mixed region at peak neutron production and the mix mass is smaller than the unshocked mass, the effect of the ablative RT mix on the target performance is small. Despite this, the target yield and peak pressure are reduced in such implosions to ~30% to 40% of the 1-D–predicted values because of the growth non-uniformities during the shell's deceleration.

To demonstrate the ignition hydrodynamic equivalence, OMEGA implosions must reach central pressures in excess of 100 Gbar. With the current laser-absorption limitations caused by CBET, the fuel adiabat in the hydro-equivalent designs must be at $\alpha < 2$ and the shell IFAR ~ 30, both of which are currently outside the shell's stability region. The target performance of such designs is significantly degraded with respect to 1-D predictions. Two-dimensional simulations using the known sources of target and illumination nonuniformities also fail to reproduce the experimental data. This limited ability of the hydrodynamic simulations to explain the observables in the low-adiabat implosions on OMEGA is also common in indirect-drive cryogenic implosions on the NIF.

To understand the factors limiting the target performance, simplified models describing implosion dynamics have been developed. Such models revealed that the vapor pressure evolution during shell acceleration and shell density relaxation caused by hydrodynamic instability growth and preheat are the main factors controlling the target performance. It was shown that 2-D *DRACO* simulations that use the localized features on the target surface as the nonuniformity seed reproduce the observables for $\alpha \simeq 2$ implosions. The shells in these simulations are totally broken, and the cold shell material, ablator, and blowoff plasma are injected into the target center, significantly reducing the final shell convergence and hot-spot pressure.

Based on the analysis using the simplified models and the simulations with the localized defects, it was concluded that ignition hydrodynamic equivalence can be achieved on OMEGA by making the cryogenic designs more robust against the hydrodynamics instabilities. This requires a reduction in nonuniformity sources and an increase in hydroefficiency by mitigating the CBET. LLE is currently pursuing several CBET-mitigation strategies, including a reduced beam size relative to the target size, an enhanced laser bandwidth, and multilayer ablators.

Appendix A: Shell Acceleration Model

The momentum–conservation equation in the mass–time coordinate system has the form

$$\frac{\partial^2 r(m,t)}{\partial t^2} = -4\pi r(m,t)^2 \frac{\partial p(m,t)}{\partial m}, \qquad (A1)$$

where p is shell pressure, r is position, m is the mass coordinate defined as $dm = 4\pi\rho r^2 dr$, and ρ is mass density. A rigorous approach for finding $r(m,t)$ requires solving a nonlinear partial differential equation by substituting $p(m,t) = \mu\alpha(m,t) / \left[4\pi r(\partial r/\partial m)^2\right]^{5/3}$ into Eq. (A1). Here, the shell's adiabat $\alpha(m,t)$ is a function of time during shell acceleration because of secondary shocks, radiation, or suprathermal electron preheat, and μ is defined in Eq. (18). Instead, an approximate solution of Eq. (A1) is obtained by using the following simplifications: First, the pressure profile inside the shell is written as a second-order polynomial in the mass coordinate,

$$p(m,t) \simeq p_a(t)\left[1 + \hat{p}_1(t)\eta + \hat{p}_2(t)\eta^2\right], \qquad (A2)$$

where $\eta = (1-m/M)$ is the normalized mass with zero value at the ablation front, p_a is the ablation pressure, and M is the total shell mass. Second, a solution of Eq. (A1) is obtained near the ablation region as an expansion in η, assuming $\eta \ll 1$. Finally, the adiabat is assumed to be determined by the early shock propagation through the shell and does not change significantly during the shell's acceleration. The relation between the position and mass is determined by substituting

$$p(m,t) = \mu\alpha\rho^{5/3} \tag{A3}$$

into the mass-conservation equation [here, μ is defined in Eq. (18)]. The result is

$$\frac{\partial r^3}{\partial m} = \frac{3\mu^{3/5}}{4\pi}\left(\frac{\alpha}{p}\right)^{3/5}. \tag{A4}$$

Next, the ablation pressure is written as a function of the ablation-front position R_a. Since the critical surface and the laser-deposition region move inward during the shell's implosion, the ablation pressure (or drive pressure) increases with the shell convergence. Assuming that the ablation pressure scales with the laser intensity as $p_a \sim I^{\beta_a}$, the pressure change with the ablation-front radius R_a becomes $p_a \sim \left(P_{laser}/R_a^2\right)^{\beta_a} = P_{laser}^{\beta_a}R_a^{-2\beta_a}$, where P_{laser} is the laser power. The power index β_a depends on the details of the laser-absorption mechanism and thermal conduction (see, for example, Ref. 48). To generalize, we write the drive pressure as $p_a \sim R_a^{-\beta}$, where the values of power index β typically range from 0.5 to 1.5 for various laser-deposition and thermal-conduction models and ablator materials. Introducing the normalized position $\xi(\eta,t) = r(\eta,t)/R_0$, where R_0 is the ablation-front position at the beginning of the shell's acceleration, the ablation pressure can be written as

$$p_a = p_{a,0}\xi_a^{-\beta} \tag{A5}$$

and Eq. (A4) takes the form

$$\frac{\partial\xi^3}{\partial\eta} = -\epsilon\xi_a^{3\beta/5}\left(\frac{\alpha/\alpha_a}{1+\hat{p}_1\eta+\hat{p}_2\eta^2}\right)^{3/5}, \tag{A6}$$

where α_a is the shell's adiabat in the ablation-front region and $\xi_a = R_a/R_0$. The small parameter ϵ is defined as

$$\epsilon = \frac{3\mu^{3/5}}{4\pi}\left(\frac{\alpha_a}{p_{a,0}}\right)^{3/5}\frac{M_{shell}}{R_0^3} = \frac{M_{shell}}{4\pi\rho_{a,0}R_0^3/3} \ll 1, \tag{A7}$$

where $p_{a,0}$ and $\rho_{a,0}$ are the ablation pressure and the peak shell density at the beginning of shell acceleration, respectively. Keeping only the terms up to the order of η, the solution of Eq. (A6) becomes

$$\xi(\eta,t) = \xi_a(t)\left[1 - \frac{\epsilon}{3}\xi_a(t)^{3\beta/5-3}\eta\right]. \tag{A8}$$

Substituting Eq. (A8) back into Eq. (A1) determines the temporal evolution of the normalized ablation-front radius ξ_a and shell pressure p:

$$\xi_a'' = \frac{4\pi R_0}{M}p_{a,0}\xi_a^{2-\beta}\hat{p}_1, \tag{A9}$$

$$\hat{p}_2 = \frac{\epsilon}{6}\xi_a^{3/5\beta-3}\left[\hat{p}_1\left(4-\frac{3}{5}\beta\right) - \frac{M}{4\pi R_0 p_{a,0}}\right.$$
$$\left.\times\left(2-\frac{3}{5}\beta\right)\left(3-\frac{3}{5}\beta\right)\frac{\xi_a'^2}{\xi_a^{3-\beta}}\right]. \tag{A10}$$

Assuming that the pressure at the inner shell boundary ($\eta = 1$) is $p(\eta = 1) = p_{bk}(t)$ ($p_{bk} \ll p_a$ during the shell acceleration) relates $\hat{p}_2$ with $\hat{p}_1$:

$$\hat{p}_1 = -1 + p_{bk}/p_a - \hat{p}_2. \tag{A11}$$

The shell pressure at the inner surface p_{bk} is determined from Eq. (29):

$$p_{bk} \simeq p_{a,0}\frac{\rho_{v,0}}{\rho_0}\left\{1 + 2\sqrt{5}\left[1 - \left(\frac{\rho_{v,0}}{\rho_0}\right)^{1/5}\right]\right\}\left(\frac{V_{bk,0}}{V_{bk}}\right), \tag{A12}$$

where V_{bk} and $V_{bk,0}$ are the volume surrounded by the inner surface of the shell and its value at the beginning of the shell's acceleration, respectively. The volume ratio in Eq. (A12) is due to the convergence effects. Then, Eq. (A10) gives

$$\hat{p}_2 = -\frac{\epsilon}{6}(4-3/5\beta)\xi_a^{3/5\beta-3}$$
$$\times\frac{\xi_a'^2/\xi_a^{3-\beta}C_\beta(M/4\pi R_0 p_{a,0}) + 1 - p_{bk}/p_a}{1+\epsilon(4-3/5\beta)\xi_a^{3/5\beta-3}/6}, \tag{A13}$$

where

$$C_\beta = \frac{(2 - 3/5\beta)(3 - 3/5\beta)}{4 - 3/5\beta}.$$

When the shell convergence is not significant ($R_a \sim R_0$, $\xi_a \sim 1$), $\hat{p}_1 \simeq -1$ and the ablation-front velocity, obtained by integrating Eq. (A9), reduces to

$$\xi'^2_a = \frac{8\pi R_0 p_{a,0}}{M} \frac{1 - \xi_a^{3-\beta}}{3 - \beta}. \qquad (A14)$$

Since the velocity gradient inside the shell is small at this stage in the implosion, the mass-averaged shell velocity v_{shell} can be approximated by the ablation-front velocity $v_{shell} \simeq \dot{R}_a = R_0 \xi'_a$. This gives the shell's kinetic energy as a function of the ablation-front radius:

$$\frac{Mv^2_{shell}}{2} = \frac{4\pi}{3 - \beta} \left[p_{a,0} R_0^3 - p_a(t) R_a^3 \right]$$

$$= \frac{4\pi}{3 - \beta} p_{a,0} R_0^3 \left[1 - \left(\frac{R_a}{R_0} \right)^{3-\beta} \right]. \qquad (A15)$$

Equation (A15) shows, as expected, that as the shell converges and R_a gets smaller, the shell's kinetic energy increases and the larger values of β [which correspond to a faster rise in the ablation pressure during the shell convergence; see Eq. (A5)] lead to increased kinetic energy. Note that Eq. (A15) is not valid for $\beta = 3$. Integrating Eq. (A9) in this case leads to

$$\frac{Mv^2_{shell}}{2} = 4\pi p_{a,0} R_0^3 \ln \frac{R_0}{R_a}, \quad \beta = 3. \qquad (A16)$$

Appendix B: Model of Shell Deceleration

1. Equation for the Hot-Spot Radius

Following the analysis used in modeling the shell's acceleration [see Eqs. (A2)–(A10)], pressure of the shocked shell is written as

$$p = p_{hs}(t) \left[1 + \hat{p}_1^{hs} \frac{m}{M} + \hat{p}_2^{hs} \left(\frac{m}{M} \right)^2 \right], \qquad (B1)$$

and the solution of Eq. (A1) is found near the inner surface of the shell as a series expansion in $m/M \ll 1$. If M_s is the mass of the

shocked shell and the pressure at the shock front is $p(M_s) = p_{shock}$, substituting $p_{hs}(t)$ from Eq. (24) into Eq. (B1 gives

$$\hat{p}_2^{hs} = -\frac{M}{6\rho_{shock,0} V_{hs,0}} \hat{p}_1^{hs}, \qquad (B2)$$

$$\hat{p}_1^{hs} = -(p_{hs} - p_{shock}) \frac{M}{M_s p_{hs}} \left(1 - \frac{M_s}{6\rho_{shock,0} V_{hs,0}} \right)^{-1}, \qquad (B3)$$

and the hot-spot radius is determined by

$$\ddot{R}_{hs} = S_{hs} \frac{p_{hs} - p_{shock}}{M_s} \left(1 - \frac{M_s}{6\rho_{shock,0} V_{hs,0}} \right)^{-1}, \qquad (B4)$$

where S_{hs} is the surface area of the hot spot and $\rho_{shock,0}$ and $V_{hs,0}$ are the shell density at the inner edge of the shell and hot-spot volume at the beginning of the shell's deceleration, respectively (see Fig. 137.32). As described earlier [see Eq. (25)], the maximum hot-spot pressure depends on the hot-spot convergence ratio during deceleration. Equation (B4) shows that the hot-spot convergence is determined by the pressure difference between the hot spot and the shock fronts, $p_{hs} - p_{shock}$, and the shocked-shell mass (the shocked mass M_s). If the vapor pressure for a given hot-spot radius is increased in an experiment compared to the code predictions (as a result of the larger vapor mass, for example), the shell's deceleration is stronger and the shocked mass is smaller. This results in a smaller fraction of the shell's kinetic energy being converted into the internal energy of the hot spot, leading to reduced hot-spot pressures.

2. Equations for the Shocked Mass and Shock Pressure

The conservation laws at the shock front are used to determine M_s and p_{shock}. The change in momentum of the shell's material as it passes through the shock surface, $-dM_s/dt(v_{shell,s} - v_{shock})$, is balanced by the pressure force, $-(p_{shell,s} - p_{shock}) S_{shock}$, yielding

$$\frac{dM_s}{dt}(v_{shell,s} - v_{shock}) = (p_{shell,s} - p_{shock}) S_{shock}, \qquad (B5)$$

where v_{shock}, p_{shock}, and $v_{shell,s} < 0$, $p_{shell,s}$ are the velocity and pressure at the shock front in the shock-compressed (region II in Fig. 137.33) and unshocked (region I in Fig. 137.33) regions, respectively, and S_{shock} is the surface area of the outgoing shock wave. The mass flux across the shock is determined from the Hugoniot conditions,[39]

$$\frac{dM_s}{dt} = \sqrt{\frac{\rho_{shell,s}}{3}} \sqrt{4p_{shock} + p_{shell,s}} \, S_{shock} . \qquad (B6)$$

Eliminating dM_s/dt from Eqs. (B5) and (B6) gives

$$p_{shock} = p_{shell,s} - \sqrt{\frac{\rho_{shell,s}}{3} \left(4p_{shock} + p_{shell,s} \right)}$$

$$\times \left(v_{shell,s} - v_{shock} \right). \qquad (B7)$$

The position of the outgoing shock wave R_{shock} is determined by

$$\frac{dR_{shock}}{dt} = \sqrt{\frac{4p_{shock} + p_{shell,s}}{3\rho_{shell,s}}} + v_{shell,s} . \qquad (B8)$$

In the strong-shock approximation $p_{shock} \gg p_{shell}$, these equations reduce to

$$\frac{dM_s}{dt} \simeq \frac{4}{3} \rho_{shell,s} \left(v_{shock} - v_{shell,s} \right) S_{shock} ,$$

$$p_{shock} \simeq \frac{4}{3} \rho_{shell,s} \left(v_{shock} - v_{shell,s} \right)^2 , \qquad (B9)$$

$$\frac{dR_{shock}}{dt} = \frac{4}{3} v_{shock} - \frac{1}{3} v_{shell,s} .$$

The shock pressure p_{shock} continues to increase while the shell converges inward. This is a result of two effects: first, an increase in shell density ahead of the shock ρ_{shell} (because of the shell's convergence); second, a decrease in the absolute value of the post-shock velocity v_{shock} caused by the shell's deceleration. The rate of increase in p_{shock} is limited, however, by the deceleration of the unshocked shell and a reduction in $|v_{shell}|$. The shell density and pressure evolutions will be discussed next.

3. Equation for the Unshocked Shell Density

The velocity gradient across the shell is calculated by taking the time derivative of Eq. (A4):

$$\frac{1}{v} \frac{\partial v}{\partial m} = -\frac{2}{3\rho(m)V(m)} \left(1 + \frac{3}{10} \frac{\partial p}{\partial t} \frac{r}{pv} \right). \qquad (B10)$$

Assuming that the velocity gradient is uniform across the shell, Eq. (B10) is evaluated at the ablation front. This gives an estimate of the velocity difference Δv across the shell:

$$\frac{\Delta v}{vM} \simeq -\frac{2}{3\rho_a V_a} \left(1 + \frac{3}{10} \frac{dp_a}{dR_a} \frac{R_a}{p_a} \right). \qquad (B11)$$

Equation (B11) shows that the velocity difference between the outer and inner parts of the shell is amplified during the implosion because of convergence ($\rho_a V_a$ decreases). This effect is absent, for example, in planar geometry where the shell's velocity profile is nearly flat. The ablation pressure scales with the ablation radius as $p_a \sim R_a^{-\beta}$ [see Eq. (A5)], leading to $dp_a/dR_a(R_a/p_a) = -\beta$. Then, Eq. (42) is used to evaluate Eq. (B11) at the end of the ablation-front acceleration, giving

$$\Delta v \simeq \sqrt{\frac{2(2 - 3/5\beta)}{(5 - \beta)}} \, c_s . \qquad (B12)$$

For the values of β relevant to the ICF implosions, $\Delta v \simeq 0.8 \, c_s$–$0.9 \, c_s$. Equation (B12) shows that at the end of the ablation-front acceleration, the velocity variation across the shell is proportional to the shell's sound speed. Therefore, as the return shock starts propagating through the shell at the beginning of the shell's deceleration, it first interacts with the shell's inner part, which moves inward with the larger velocity. Then, as the shock travels through the shell, the incoming shell velocity at the shock front decreases with time because of the velocity gradient shown in Eq. (B12). An additional decrease in the incoming shell velocity is caused by the pressure gradient that creates a force decelerating the unshocked shell.

To calculate the pressure gradient and the density evolution in the unshocked shell, the mass-conservation equation is used:

$$\frac{\partial}{\partial t} \left(\frac{1}{\rho r^2} \right) = 4\pi \frac{\partial v}{\partial m} . \qquad (B13)$$

Then, substituting $\partial v/\partial m \simeq \Delta v/M$ and using Eq. (B12) gives

$$\rho(m,t) \simeq \rho_0(m) \left[\frac{r_0(m)}{r(m,t)} \right]^2$$

$$\times \left[1 + 4\pi C_d \frac{c_{s,0}}{M} (t - t_d) \rho_0(m) r_0(m)^2 \right]^{-1} , \quad (B14)$$

where the coefficient $C_d = \sqrt{2(2 - 3/5\beta)/(5 - \beta)}$ ranges from 0.8 to 0.9 for the values of β relevant to the direct-drive implo-

sions, $c_{s,0}$ is the shell's sound speed at the beginning of deceleration, $\rho_0(m)$ and $r_0(m)$ are the shell's density and position, respectively, as functions of mass coordinate at the beginning of shell deceleration, and t_d is the starting time of shell deceleration. Strictly speaking, the velocity gradient $\Delta v/M$ is not a constant. It increases during shell deceleration because of the pressure gradient along the radial direction. This pressure gradient decelerates the ablation-front region, increasing Δv. Consequently, Eq. (B14) overestimates the density increase. Results of the hydrodynamic simulations indicate, however, that Eq. (B14) is accurate within a few-percent error.

4. Equations for the Unshocked Shell Velocity and Pressure

The velocity slowdown ahead of the outgoing shock wave is calculated using $dv_{shell}/dt \sim -S_{shock}\,\partial p/\partial m$. Assuming that the shell adiabat does not change significantly inside the unshocked shell, the shell pressure is calculated by substituting Eq. (B14) into $p \sim \rho^{5/3}$, giving

$$p_{shell} \simeq p_0(m)\left[\frac{r_0(m)}{r(m,t)}\right]^{10/3}\Sigma^{-5/3},$$

(B15)

$$\Sigma = 1 + 4\pi C_d \frac{c_{s,0}}{M}(t-t_d)\rho_0(m)r_0(m)^2,$$

and the pressure gradient becomes

$$\frac{\partial p}{\partial m} \simeq \left(\frac{r_0}{r}\right)^{10/3}\Sigma^{-8/3}\left(\frac{\partial p_0}{\partial m} + \frac{5p_0}{6\pi\rho_0 r_0^3}\right)$$

$$-\left(\frac{r_0}{r}\right)^{13/3}\Sigma^{-2/3}\frac{5p_0}{6\pi\rho_0 r_0^3}.$$

(B16)

5. Relation Between the Post-Shock Velocity and the Hot-Spot Convergence Rate

To complete defining the model for the shell's deceleration and the hot-spot formation, the hot-spot convergence rate $\dot{R}_{hs}$ must be related to the post-shock velocity v_{shock}. This is accomplished using the mass-conservation equation in the form shown in Eq. (B13). The shell's density at the inner edge of the shell satisfies $\rho_{shell}V_{hs} = $ const. Therefore,

$$\frac{\dot{R}_{hs}}{3\rho_{shock,0}V_{hs,0}} \simeq \frac{v_{shock}-\dot{R}_{hs}}{M_s}$$

(B17)

and the shocked-shell velocity at the shock front becomes

$$v_{shock} = \dot{R}_{hs}\left(1 + \frac{M_s}{3\rho_{shock,0}V_{hs,0}}\right).$$

(B18)

Since $\dot{R}_{hs} < 0$ prior to shell stagnation, the velocity gradient is negative inside the shock-compressed region.

REFERENCES

1. J. D. Lindl, *Inertial Confinement Fusion: The Quest for Ignition and Energy Gain Using Indirect Drive* (Springer-Verlag, New York, 1998).

2. S. Atzeni and J. Meyer-ter-Vehn, *The Physics of Inertial Fusion: Beam Plasma Interaction, Hydrodynamics, Hot Dense Matter*, International Series of Monographs on Physics (Clarendon Press, Oxford, 2004).

3. R. Betti, K. Anderson, V. N. Goncharov, R. L. McCrory, D. D. Meyerhofer, S. Skupsky, and R. P. J. Town, Phys. Plasmas **9**, 2277 (2002).

4. V. N. Goncharov, in *Laser-Plasma Interactions*, edited by D. A. Jaroszynski, R. Bingham, and R. A. Cairns, Scottish Graduate Series (CRC Press, Boca Raton, FL, 2009), pp. 409–418.

5. S. Chandrasekhar, *Hydrodynamic and Hydromagnetic Stability*, International Series of Monographs on Physics (Dover Publications, New York, 1981), Chap. X, pp. 428–480.

6. J. Sanz, Phys. Rev. Lett. **73**, 2700 (1994); V. N. Goncharov, R. Betti, R. L. McCrory, P. Sorotokin, and C. P. Verdon, Phys. Plasmas **3**, 1402 (1996).

7. T. R. Boehly, D. L. Brown, R. S. Craxton, R. L. Keck, J. P. Knauer, J. H. Kelly, T. J. Kessler, S. A. Kumpan, S. J. Loucks, S. A. Letzring, F. J. Marshall, R. L. McCrory, S. F. B. Morse, W. Seka, J. M. Soures, and C. P. Verdon, Opt. Commun. **133**, 495 (1997).

8. V. N. Goncharov, T. C. Sangster, T. R. Boehly, S. X. Hu, I. V. Igumenshchev, F. J. Marshall, R. L. McCrory, D. D. Meyerhofer, P. B. Radha, W. Seka, S. Skupsky, C. Stoeckl, D. T. Casey, J. A. Frenje, and R. D. Petrasso, Phys. Rev. Lett. **104**, 165001 (2010).

9. J. Delettrez, R. Epstein, M. C. Richardson, P. A. Jaanimagi, and B. L. Henke, Phys. Rev. A **36**, 3926 (1987).

10. V. N. Goncharov, T. C. Sangster, P. B. Radha, R. Betti, T. R. Boehly, T. J. B. Collins, R. S. Craxton, J. A. Delettrez, R. Epstein, V. Yu. Glebov, S. X. Hu, I. V. Igumenshchev, J. P. Knauer, S. J. Loucks, J. A. Marozas, F. J. Marshall, R. L. McCrory, P. W. McKenty, D. D. Meyerhofer, S. P. Regan, W. Seka, S. Skupsky, V. A. Smalyuk, J. M. Soures, C. Stoeckl, D. Shvarts, J. A. Frenje, R. D. Petrasso, C. K. Li, F. Séguin, W. Manheimer, and D. G. Colombant, Phys. Plasmas **15**, 056310 (2008).

11. I. V. Igumenshchev, D. H. Edgell, V. N. Goncharov, J. A. Delettrez, A. V. Maximov, J. F. Myatt, W. Seka, A. Shvydky, S. Skupsky, and C. Stoeckl, Phys. Plasmas **17**, 122708 (2010).

12. I. V. Igumenshchev, W. Seka, D. H. Edgell, D. T. Michel, D. H. Froula, V. N. Goncharov, R. S. Craxton, L. Divol, R. Epstein, R. Follett, J. H.

Kelly, T. Z. Kosc, A. V. Maximov, R. L. McCrory, D. D. Meyerhofer, P. Michel, J. F. Myatt, T. C. Sangster, A. Shvydky, S. Skupsky, and C. Stoeckl, Phys. Plasmas **19**, 056314 (2012).

13. C. J. Randall, J. R. Albritton, and J. J. Thomson, Phys. Fluids **24**, 1474 (1981).

14. W. L. Kruer, in *The Physics of Laser Plasma Interactions, Frontiers in Physics*, Vol. 73, edited by D. Pines (Addison-Wesley, Redwood City, CA, 1988).

15. A. Simon, R. W. Short, E. A. Williams, and T. Dewandre, Phys. Fluids **26**, 3107 (1983).

16. J. F. Myatt, H. X. Vu, D. F. DuBois, D. A. Russell, J. Zhang, R. W. Short, and A. V. Maximov, Phys. Plasmas **20**, 052705 (2013).

17. W. M. Manheimer, D. G. Colombant, and J. H. Gardner, Phys. Fluids **25**, 1644 (1982).

18. D. T. Michel, C. Sorce, R. Epstein, N. Whiting, I. V. Igumenshchev, R. Jungquist, and D. H. Froula, Rev. Sci. Instrum. **83**, 10E530 (2012).

19. D. T. Michel, V. N. Goncharov, I. V. Igumenshchev, R. Epstein, and D. H. Froula, Phys. Rev. Lett. **111**, 245005 (2013).

20. W. Seka, D. H. Edgell, J. P. Knauer, J. F. Myatt, A. V. Maximov, R. W. Short, T. C. Sangster, C. Stoeckl, R. E. Bahr, R. S. Craxton, J. A. Delettrez, V. N. Goncharov, I. V. Igumenshchev, and D. Shvarts, Phys. Plasmas **15**, 056312 (2008).

21. T. Dewandre, J. R. Albritton, and E. A. Williams, Phys. Fluids **24**, 528 (1981).

22. S. Skupsky, R. W. Short, T. Kessler, R. S. Craxton, S. Letzring, and J. M. Soures, J. Appl. Phys. **66**, 3456 (1989).

23. *LLE Review Quarterly Report* **130**, 72, Laboratory for Laser Energetics, University of Rochester, Rochester, NY, LLE Document No. DOE/NA/28302-1058 (2012).

24. V. N. Goncharov, in *Laser-Plasma Interactions and Applications*, edited by P. McKenna, D. Neely, R. Bingham, and D. A. Jaroszynski, Scottish Graduate Series (Springer, Switzerland, 2013), Chap. 7, pp. 135–183.

25. H. Brysk, Plasma Phys. **15**, 611 (1973).

26. T. C. Sangster, V. N. Goncharov, R. Betti, P. B. Radha, T. R. Boehly, D. T. Casey, T. J. B. Collins, R. S. Craxton, J. A. Delettrez, D. H. Edgell, R. Epstein, C. J. Forrest, J. A. Frenje, D. H. Froula, M. Gatu-Johnson, V. Yu. Glebov, D. R. Harding, M. Hohenberger, S. X. Hu, I. V. Igumenshchev, R. Janezic, J. H. Kelly, T. J. Kessler, C. Kingsley, T. Z. Kosc, J. P. Knauer, S. J. Loucks, J. A. Marozas, F. J. Marshall, A. V. Maximov, R. L. McCrory, P. W. McKenty, D. D. Meyerhofer, D. T. Michel, J. F. Myatt, R. D. Petrasso, S. P. Regan, W. Seka, W. T. Shmayda, R. W. Short, A. Shvydky, S. Skupsky, J. M. Soures, C. Stoeckl, W. Theobald, V. Versteeg, B. Yaakobi, and J. D. Zuegel, Phys. Plasmas **20**, 056317 (2013).

27. J. A. Frenje, C. K. Li, F. H. Séguin, D. T. Casey, R. D. Petrasso, T. C. Sangster, R. Betti, V. Yu. Glebov, and D. D. Meyerhofer, Phys. Plasmas **16**, 042704 (2009); J. A. Frenje, D. T. Casey, C. K. Li, F. H. Séguin, R. D.

Petrasso, V. Yu. Glebov, P. B. Radha, T. C. Sangster, D. D. Meyerhofer, S. P. Hatchett, S. W. Haan, C. J. Cerjan, O. L. Landen, K. A. Fletcher, and R. J. Leeper, Phys. Plasmas **17**, 056311 (2010).

28. C. J. Forrest, P. B. Radha, V. Yu. Glebov, V. N. Goncharov, J. P. Knauer, A. Pruyne, M. Romanofsky, T. C. Sangster, M. J. Shoup III, C. Stoeckl, D. T. Casey, M. Gatu-Johnson, and S. Gardner, Rev. Sci. Instrum. **83**, 10D919 (2012).

29. C. Stoeckl, V. Yu. Glebov, S. Roberts, T. C. Sangster, R. A. Lerche, R. L. Griffith, and C. Sorce, Rev. Sci. Instrum. **74**, 1713 (2003).

30. C. Cerjan, P. T. Springer, and S. M. Sepke, Phys. Plasmas **20**, 056319 (2013).

31. P. B. Radha, V. N. Goncharov, T. J. B. Collins, J. A. Delettrez, Y. Elbaz, V. Yu. Glebov, R. L. Keck, D. E. Keller, J. P. Knauer, J. A. Marozas, F. J. Marshall, P. W. McKenty, D. D. Meyerhofer, S. P. Regan, T. C. Sangster, D. Shvarts, S. Skupsky, Y. Srebro, R. P. J. Town, and C. Stoeckl, Phys. Plasmas **12**, 032702 (2005).

32. S. X. Hu, P. B. Radha, V. N. Goncharov, R. Betti, R. Epstein, F. J. Marshall, R. L. McCrory, D. D. Meyerhofer, T. C. Sangster, and S. Skupsky, Bull. Am. Phys. Soc. **58**, 324 (2013).

33. Prism Computational Sciences, Inc., Madison, WI 53711; J. J. MacFarlane *et al.*, High Energy Density Phys. **3**, 181 (2007).

34. F. J. Marshall and J. A. Oertel, Rev. Sci. Instrum. **68**, 735 (1997).

35. M. J. Edwards, P. K. Patel, J. D. Lindl, L. J. Atherton, S. H. Glenzer, S. W. Haan, J. D. Kilkenny, O. L. Landen, E. I. Moses, A. Nikroo, R. Petrasso, T. C. Sangster, P. T. Springer, S. Batha, R. Benedetti, L. Bernstein, R. Betti, D. L. Bleuel, T. R. Boehly, D. K. Bradley, J. A. Caggiano, D. A. Callahan, P. M. Celliers, C. J. Cerjan, K. C. Chen, D. S. Clark, G. W. Collins, E. L. Dewald, L. Divol, S. Dixit, T. Doeppner, D. H. Edgell, J. E. Fair, M. Farrell, R. J. Fortner, J. Frenje, M. G. Gatu Johnson, E. Giraldez, V. Yu. Glebov, G. Grim, B. A. Hammel, A. V. Hamza, D. R. Harding, S. P. Hatchett, N. Hein, H. W. Herrmann, D. Hicks, D. E. Hinkel, M. Hoppe, W. W. Hsing, N. Izumi, B. Jacoby, O. S. Jones, D. Kalantar, R. Kauffman, J. L. Kline, J. P. Knauer, J. A. Koch, B. J. Kozioziemski, G. Kyrala, K. N. LaFortune, S. Le Pape, R. J. Leeper, R. Lerche, T. Ma, B. J. MacGowan, A. J. MacKinnon, A. Macphee, E. R. Mapoles, M. M. Marinak, M. Mauldin, P. W. McKenty, M. Meezan, P. A. Michel, J. Milovich, J. D. Moody, M. Moran, D. H. Munro, C. L. Olson, K. Opachich, A. E. Pak, T. Parham, H.-S. Park, J. E. Ralph, S. P. Regan, B. Remington, H. Rinderknecht, H. F. Robey, M. Rosen, S. Ross, J. D. Salmonson, J. Sater, D. H. Schneider, F. H. Séguin, S. M. Sepke, D. A. Shaughnessy, V. A. Smalyuk, B. K. Spears, C. Stoeckl, W. Stoeffl, L. Suter, C. A. Thomas, R. Tommasini, R. P. Town, S. V. Weber, P. J. Wegner, K. Widman, M. Wilke, D. C. Wilson, C. B. Yeamans, and A. Zylstra, Phys. Plasmas **20**, 070501 (2013).

36. J. Paisner *et al.*, Laser Focus World **30**, 75 (1994).

37. Von G. Guderley, Luftfahrtforschung **19**, 302 (1942).

38. C. Bellei *et al.*, Phys. Plasmas **20**, 012701 (2013); C. Bellei *et al.*, Phys. Plasmas **20**, 044702 (2013).

39. L. D. Landau and E. M. Lifshits, *Fluid Mechanics* (Pergamon, Oxford, 1982).

40. I. V. Igumenshchev, V. N. Goncharov, W. T. Shmayda, D. R. Harding, T. C. Sangster, and D. D. Meyerhofer, Phys. Plasmas **20**, 082703 (2013).

41. R. Betti and J. Sanz, Phys. Rev. Lett. **97**, 205002 (2006).

42. D. Layzer, Astrophys. J. **122**, 1 (1955); D. Oron *et al.*, Phys. Plasmas **8**, 2883 (2001); V. N. Goncharov, Phys. Rev. Lett. **88**, 134502 (2002).

43. D. H. Edgell, W. Seka, R. E. Bahr, T. R. Boehly, and M. J. Bonino, Phys. Plasmas **15**, 092704 (2008).

44. M. C. Herrmann, M. Tabak, and J. D. Lindl, Phys. Plasmas **8**, 2296 (2001).

45. I. V. Igumenshchev, D. H. Froula, D. H. Edgell, V. N. Goncharov, T. J. Kessler, F. J. Marshall, R. L. McCrory, P. W. McKenty, D. D. Meyerhofer, D. T. Michel, T. C. Sangster, W. Seka, and S. Skupsky, Phys. Rev. Lett. **110**, 145001 (2013); D. H. Froula, T. J. Kessler, I. V. Igumenshchev, R. Betti, V. N. Goncharov, H. Huang, S. X. Hu, E. Hill, J. H. Kelly, D. D. Meyerhofer, A. Shvydky, and J. D. Zuegel, Phys. Plasmas **20**, 082704 (2013).

46. S. X. Hu, G. Fiksel, V. N. Goncharov, S. Skupsky, D. D. Meyerhofer, and V. A. Smalyuk, Phys. Rev. Lett. **108**, 195003 (2012); G. Fiksel, S. X. Hu, V. N. Goncharov, D. D. Meyerhofer, T. C. Sangster, V. A. Smalyuk, B. Yaakobi, M. J. Bonino, and R. Jungquist, Phys. Plasmas **19**, 062704 (2012).

47. R. J. Henchen, V. N. Goncharov, D. T. Michel, R. K. Follett, J. Katz, and D. H. Froula, Bull. Am. Phys. Soc. **58**, 151 (2013).

48. C. E. Max, C. F. McKee, and W. C. Mead, Phys. Fluids **23**, 1620 (1980).